ADVANCED MATERIALS
www.advmat.de

Approaching Standardization: Mechanical Material Testing of Macroscopic Two-Photon Polymerized Specimens

Thomas Koch, Wenxin Zhang, Thomas T. Tran, Yingjin Wang, Adrian Mikitisin, Jakob Puchhammer, Julia R. Greer, Aleksandr Ovsianikov,* Franziska Chalupa-Gantner,* and Markus Lunzer**

Two-photon polymerization (2PP) is becoming increasingly established as additive manufacturing technology for microfabrication due to its high-resolution and the feasibility of generating complex parts. Until now, the high resolution of 2PP is also its bottleneck, as it limited throughput and therefore restricted the application to the production of microparts. Thus, mechanical properties of 2PP materials can only be characterized using nonstandardized specialized microtesting methods. Due to recent advances in 2PP technology, it is now possible to produce parts in the size of several millimeters to even centimeters, finally permitting the fabrication of macrosized testing specimens. Besides suitable hardware systems, 2PP materials exhibiting favorable mechanical properties that allow printing of up-scaled parts are strongly demanded. In this work, the up-scalability of three different photopolymers is investigated using a high-throughput 2PP system and low numerical aperture optics. Testing specimens in the cm-range are produced and tested with common or even standardized material testing methods available in conventionally equipped polymer testing labs. Examples of the characterization of mechanical, thermo-mechanical, and fracture properties of 2PP processed materials are shown. Additionally, aspects such as postprocessing and aging are investigated. This lays a foundation for future expansion of the 2PP technology to broader industrial application.

1. Introduction

Two-photon polymerization (2PP) is a powerful high-resolution additive manufacturing technology that covers a broad range of dimensions, including the nano-, micro-, and mesoscale. 2PP takes advantage of the nonlinear nature of two-photon absorption to reach high-resolution features.[1–3] By focusing a pulsed laser with a microscope objective and scanning the focal point, solid polymer is cured from photopolymer resin only within the laser focus.[3] This distinct volume is called the polymerization voxel. The dimensions of the voxel determine the achievable feature resolution and the throughput, which is defined as the polymerized volume per time. Those two characteristics show a reciprocal correlation and need to be balanced in accordance with the targeted fabrication quality. The size of the polymerization voxel depends on the numerical aperture (NA) of the objective, the processing parameters and the reactivity and nature of the 2PP resin.[4,5] Further, the field number and magnification of the objective define the field of view (FoV), which can be scanned at a time.[6] By choosing an adequate objective, the focal spot size and FoV can be adapted to match the targeted part dimension as well as feature resolution. In general, the throughput can be increased in reducing the amount of scan operations by increasing the voxel spacing or scanning fewer FoVs.

Since the introduction of 2PP in the 1990s,[2,5] mainly, three process development and research trends can be observed. While some studies focus on advancing resolution and

T. Koch, J. Puchhammer, A. Ovsianikov, F. Chalupa-Gantner
Institute of Materials Science and Technology
TU Wien, Vienna 1060, Austria
E-mail: thomas.koch@tuwien.ac.at; aleksandr.ovsianikov@tuwien.ac.at; franziska.gantner@tuwien.ac.at

The ORCID identification number(s) for the author(s) of this article can be found under https://doi.org/10.1002/adma.202308497

DOI: 10.1002/adma.202308497

W. Zhang, T. T. Tran, Y. Wang, J. R. Greer
Division of Engineering and Applied Sciences
California Institute of Technology
Pasadena, CA 91125, USA

A. Mikitisin
Central Facility for Electron Microscopy
RWTH Aachen, 52074 Aachen, Germany

J. R. Greer
Kavli Nanoscience Institute
California Institute of Technology
Pasadena, CA 91125, USA

M. Lunzer
UpNano GmbH
Vienna 1030, Austria
E-mail: markus.lunzer@upnano.com

precision,[7–11] others aim to improve the reactivity of the printing materials[5,12–14] or increase the writing speed and throughput of the technology.[15–26] Especially the latter is a substantial prerequisite for industrial relevance and promotes the persistent market presence of this relatively young technology. Initially, most academic research was conducted on experimental setups. Now, several commercial systems are available that operate either at a wavelength of ≈520 nm (green light, Microlight3D,[11] Multiphoton Optics,[27] Femtika[28]) or ≈780 nm (near infrared light, UpNano,[29] Nanoscribe[30]).

With the increasing availability of commercial 2PP systems and with regard to industrial applications, the mechanical characterization of 2PP materials becomes crucial. So far, in literature, experimental approaches to determine the mechanical properties of 2PP produced parts have almost always been reported on the microscale due to the low achievable throughput of 2PP in the past. For example, compliant microbeams were bent by calibrated AFM cantilevers[31,32] or optical tweezers.[33] Tensile[34-36] and compression tests[34-37] were performed using special ×or piezo microtesting equipment, often as optional upgrades of nanoindentation devices. Further, nanoindentation devices were used for the conventional determination of modulus and hardness by indentation of compact specimens,[36,38-42] but also for compression testing of bulk[34,36,37,43] and lattice structures,[43-48] or for bending of relatively stiff microbeams.[49] Even nanodynamic-mechanical analysis was performed at room temperature at constant[50] or varying frequency.[51] Moreover, AFM-based indentation was often applied to characterize 2PP printed soft biomaterials.[52-55] Besides these rather common testing methods for 2PP structures, very customized methods can be found, ranging from tensile tests of nanosprings,[56] oscillation of drum-like structures,[57] and microbeams,[58] bending recovery of nanowires[59] to the determination of the critical length of collapse under capillary drying forces.[60] Even a microparticle impact test on lattice carbon structures[61] or tensile tests on woven structures[62] were demonstrated. Recently, laser-induced resonant acoustic spectroscopy (LIRAS) has been presented for nondestructive measurement of dynamic material properties.[63] In all of those cases, suitable microtest equipment is needed, and often the data analysis seems relatively complex. Moreover, micromechanical testing is quite sensitive to thermal fluctuations and accessing thermo-mechanical properties is hardly possible.

Besides high-precision printing, the latest generation of commercial 2PP systems also allows high throughput production and thus permits the fabrication of large structures of up to several cm.[64-67] This is achieved by the use of appropriate optics (10× or even 5× magnification), high-power lasers, high-speed scanners, adaptive resolution, and optimized scanning strategies. Scanning speeds of up to meters per second, voxel rates of several million per second, and building rates of several tens to more than hundred $mm^3\ h^{-1}$ are now possible (Table 2). These substantial improvements of 2PP permit to close the gap to other additive manufacturing or conventional fabrication technologies in the meso- and macrorange.

The advances in 2PP technology demand materials suitable for up-scaled 2PP fabrication. A literature overview of photopolymers suitable for rapid 2PP processing was given by Kiefer et al. in late 2020.[13] Additional developments have been shown in the meantime.[14,12,68,69] All these studies target the improvement of processability by examining and evaluating novel photoinitiator systems or resin systems that go beyond (meth)acrylate chemistry, as Barner-Kowollik et al.[70] suggested. However, besides the general processability, the mechanical performance of 2PP materials is a critical aspect for up-scaling. In particular, the strength and fracture behavior should be in focus for meso- and macroscale applications. Not all photopolymers that work well for nano- and microscale 3D printing, which requires high crosslinking density, can be printed at a larger scale. Due to substantial shrinkage stress, such highly crosslinked material systems will very likely exhibit warping or even cracks when being used for realization of large structures.

Those challenges, along with some studies,[71,72] point to the importance of performing mechanical testing of 2PP-processed materials at larger scales. In ref. [73], microtensile tests on stitched log-pile specimens were used to create a base to further optimize the mechanical behavior of lattice structures with larger dimensions. Two publications deal with the up-scalability of microtension and microcompression tests by comparison to the behavior of bulk macroscopic material.[34,36] While the strain rate and temperature dependence of the commercial acrylate-based photopolymer IP-Dip (Nanoscribe) were compared to literature data of PMMA by Rohbeck et al.,[36] Bauer et al. compared microtest results with casted and subsequently UV-cured bulk samples made from the same photopolymer.[34] The strain rate dependency of the compressive yield strength of micropillars and of PMMA at the macroscale was comparable. In ref. [34], a decrease in double bond conversion, Young's modulus, and compressive yield strength was observed when increasing the edge length of the compression specimens from 20 to 50 µm. Still, the values are in the range of conventionally UV-cured molded macroscopic specimens. Bending tests on millimeter-sized 2PP specimens (7 mm × 0.65 mm × 0.25 mm) from a shape-memory thiol-vinyl material, fabricated with a 25× objective and 14 mm s^{-1} scanning speed were shown,[74] building time ≈17 h.[74] The obtained mechanical values were in the range of microsized objects.

Nevertheless, to the best of our knowledge, the mechanical behavior of 2PP-fabricated bulk specimens in the mm- to cm-range has not been thoroughly investigated so far. However, the application of standardized test procedures for 2PP materials would be especially important to advance the industrial use of the technology. Upscaling 2PP test specimens is crucial for developing reliable 2PP materials for the manufacturing of high-resolution parts in the mm- to cm regime. The mechanical behavior cannot be presumed or extrapolated from miniaturized microscale test experiments alone. It is unknown how the cross-linking density and inhomogeneities within the polymer network influence the mechanical properties of larger volume parts. For example, polymerization shrinkage and resulting intrinsic stresses can negatively affect the behavior of thick-walled objects, leading to cracks warpage (see ETA/TTA below).

Moreover, for the generation of larger parts that exceed the size of a FoV, several FoV need to be stitched together. The influence of these stitches on the mechanical behavior of a part has to be considered as well. Furthermore, the stability of the 2PP system as well as the fabrication process can influence the test results. Moreover, to assess the 2PP process stability, the specimen strength under tensile and bending conditions is particularly useful. Compared to results from compression

or indentation testing, these parameters are more sensitive to specimen imperfections such as microbubbles, microcracks, surface roughness, and notches, which strongly depend on the system stability and processing parameters.

At the moment, it is still unclear, if photopolymer resins, which are used for 2PP 3D printing of microsized parts at low processing speeds, can be translated to larger-scale 2PP printing and if these resins are suitable for generating meso- and macrosized parts. Hence, several questions need to be answered

1) Is the processing window of the 2PP resin large enough to guarantee relatively easy and robust processing?
2) Are the processing parameters required suitable for producing large bulk parts?
3) Can the same material be used on different size scales with different objectives?
4) What are the mechanical properties after processing and can they be translated from one objective to the other?
5) Does the stitching overlap affect the mechanical properties of a 2PP part?

In this work, we explore these questions and provide an insight into the scalability of 2PP by comprehensively studying the mechanical properties of meso- and macroscale 2PP-produced test specimens. For the first time, ISO-standardized tests for 3D printed specimens were performed on 2PP fabricated specimens. The applied high-resolution 3D printing system NanoOne allows a built height of up to 40 mm using vat polymerization, making it possible to fabricate standardized mechanical tensile testing specimens (size 5B according to ISO 527-2:2012: length of 35 mm,[75] which represents z-height in our processing case). Due to the exceptionally high throughput provided by the coarse mode, in which the width of the voxel can be increased by a factor of up to 10 (Figures S1 and S2, Supporting Information),[64] these for 2PP fabrication quite large specimens can be produced in batches in feasible build times. The latter is necessary for fabricating a sufficiently high number of samples to provide statistical relevance, as well as to perform quality assurance or optimization of process parameters by screening.

Figure 1a,b gives a rough overview of relevant studies in the field of mechanical testing of 2PP materials regarding the dimensions of the tested specimens, used objective magnifications, applied scanning speed, and loading types. For comparison, the parameters of the present work have been included, showing both scanning speed and specimen dimensions are increased by at least five times here. Note that the indicated scanning speeds represent the processing parameters applied in these cited works, not the maximum speeds of the respective 2PP systems. Figure 1c summarizes the processing conditions used in this work in more detail. Based on a preliminary study conducted a decade ago,[49] we accelerate the printing process using a high NA objective (40× / NA 1.4). In screening peak power intensities I_{peak}, we identified ideal polymerization conditions regarding resulting mechanical properties. These I_{peak} were then used to translate the power increments onto parameters that can be used for low NA objectives (10× / NA 0.4 and 5× / NA 0.25). Following this principle allowed us to investigate the scalability of the 2PP process. Moreover, this approach facilitated translating microscopic testing methods to macroscopic and standardized testing methods for the first time. [ISO 527-2:2012,[75] ISO 868:2003,[76] ISO 2039-1:2003.[77]

2. Experimental Section

2.1. Materials

2-Propanol (IPA) and acetone, both in synthesis grade, were purchased from Carl Roth (Germany). The UV-photoinitiator TPO-L (ethyl (2,4,6-trimethylbenzoyl)phenyl phosphinate, CAS: 84434-11-7) was purchased from Carbosynth Limited (UK). Acrylate resins trimethylolpropane triacrylate (TTA, SR351, CAS 15625-89-5) and ethoxylated-(20/3)-trimethylolpropane triacrylate (ETA, SR 415, CAS 28961-43-5) were received from Sartomer Europe (France). All substances purchased from commercial sources were used as received without further purification. The two-photon initiator BMOA-1T (4,4′-(2,5-thiophenediyl)bis[*N*,*N*-bis(4-methoxyphenyl)benzenamine], CAS: 2093164-71-5) was synthesized following a procedure described in literature.[79] The respective 2PP reference resin ETA/TTA was formulated by dissolving BMOA-1T (10 µmol g^{-1}, 0.69 wt%) in a 1:1 w/w mixture of ETA and TTA. Acetone was used as a cosolvent and later removed in vacuum. The commercial 2PP resins UpPhoto and UpDraft, as well as borosilicate glass substrates were provided by UpNano GmbH (Austria). For UV-casting and LCD stereolithogrpahy, formulations of TPO-L (32 µmol g^{-1}, 1 wt%) in the respective base resin (ETA/TTA, UpPhoto, UpDraft) without 2PP initiator were provided by UpNano GmbH. Glass substrates were surface modified with methacrylate groups prior to use by silanization chemistry.[55] Silicone substrates were cleaved from a CZ-Si waver (500 µm thickness, p-type), purchased from MicroChemicals GmbH (Germany), after scoring with a glass cutter. Si substrates were surface modified using a procedure described by Helmer et al.[80] Clear Resin V4 was purchased from Formlabs Inc. (MA, USA).

2.2. Specimen Preparation

2.2.1. Two-Photon Polymerization

Figure 2 illustrates the fabrication process of 2PP 3D printed specimens. The specimens were fabricated using a NanoOne 1000 high-resolution 3D printing system (UpNano GmbH, Austria) in vat mode. Here, the laser (80 MHz repetition rate, 90 fs pulse length, and 780 nm wavelength) is focused through a high-precision cover glass into a resin vat and maintained at a constant height above the bottom of the vat. Similar to continuous liquid interface production (CLIP), where a photopolymerization "dead zone" is created by controlled oxygen inhibition via diffusion through an oxygen-permeable window between the substrate and the bottom of the material reservoir,[81] a persistent liquid interface is present in vat mode. Continuous part production via optical photopolymerization is possible as no polymerization occurs outside the voxel boundaries. Although the voxel can be freely moved within the resin in 2PP, technically, a part is printed layer-by-layer. Similar to stereolithography, a galvanometer scanner positions the beam along the x,y-planes. At the same

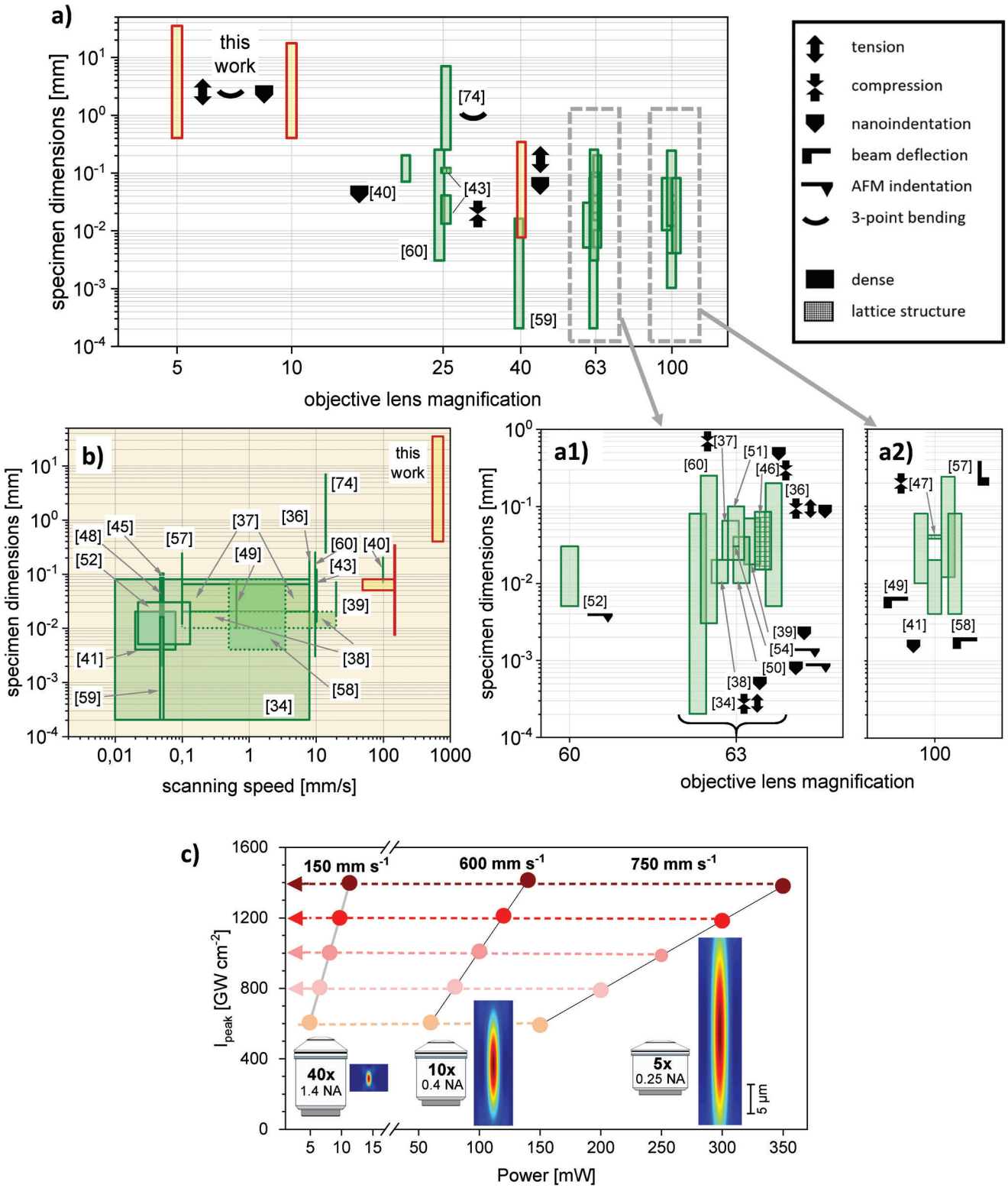

Figure 1. Overview of the state-of-the-art and scalability of 2PP processing, based on publications focusing on the mechanical testing of 2PP fabricated structures. The studies have been classified regarding specimen size and a) objective magnifications or b) scanning speed used. The applied loading types are highlighted as pictograms in (a) and the respective insets. c) Details of the processing conditions of the present work. By translating the peak power intensities I_{peak} between the different objectives, comparable processing conditions could be provided for different voxel sizes. The depicted voxel dimensions are estimated based on the FWHM, assuming a 2PP wavelength λ of 780 nm and a resin refractive index $n = 1.486$.[79]

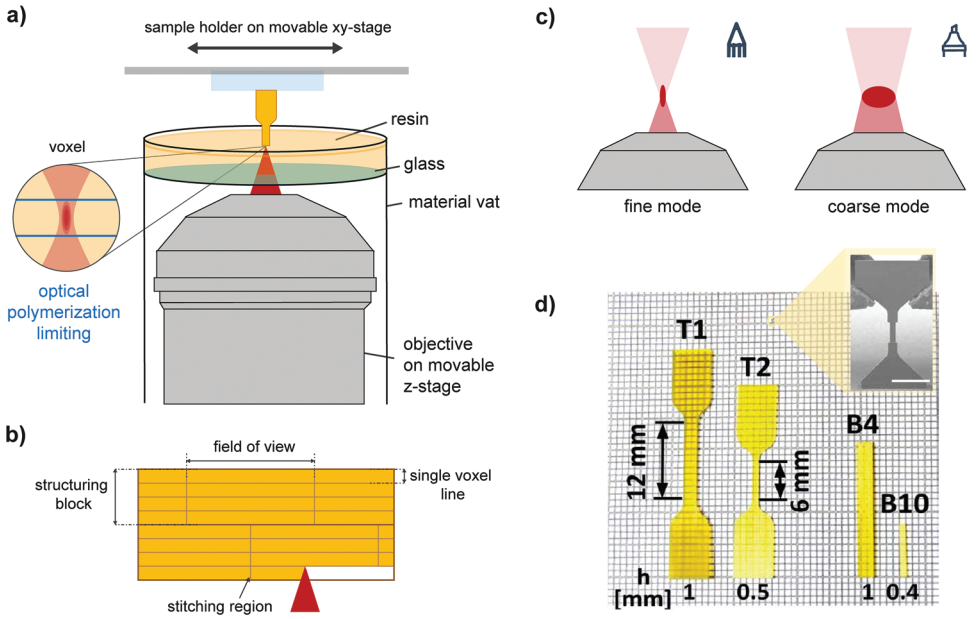

Figure 2. Illustration of the 2PP fabrication process of the test specimens. a) In vat mode the laser is focused through a high-precision cover glass into a resin vat and maintained at a constant height in the 2PP resin. Polymerization only occurs within the voxel boundaries. A liquid resin film between part and vat bottom is continuously maintained and no separation forces affect the part. Due to the 2PP inherent optical polymerization limit no light-absorbers need to be added to the resin. b) The structures are printed in a layer-wise manner. A galvanometer scanner scans the voxel along the xy-planes, while the objective and the vat are lowered along the *z*-axis. If the footprint of a part exceeds a FoV, the part is printed in consecutive blocks.[83] Blocks are defined in x,y-direction by the size of the field of view (FoV) and in z-direction by the height, which still allows printing directly next to an existing block without shadowing at the interface. In the stitching region the FoVs are slightly overlapped to increase the interconnection. c) Fine mode enables high resolution printing, whereas the voxel is enlarged in coarse mode to allow higher throughput, as the line spacing can be further increased (Figures S1 and S2, Supporting Information). d) Overview of the 2PP printed tensile and bending test specimens T1, T2, B4, and B10. Using the 5× objective and coarse mode a batch of six B10 specimens is printed in less than 15 min, a batch of six T1 specimens in 530 min. Grid spacing in mm. Additionally, a microsized tensile specimen is shown for comparison. Scale bar 100 µm.

time, the objective and the vat are lowered along the *z*-axis using a piezo-stage (Figure 2b) for layer-wise 3D printing.[82]

The following microscope objectives were used: a 40× oil immersion objective (NA 1.4, UPlanXApo 40x, Olympus), a 10× air objective (NA 0.4, UPLXAPO 10x, Olympus), and a 5× air objective (NA 0.25, Fluar 5x/0.25, Zeiss). Methacrylized borosilicate glass was used as substrate. Depending on the objective different laser powers, scanning speeds, line distances (d_{xy}), and layer spacings (d_z) were applied (see **Table 1**). Tensile test specimens as well as notched bending specimens were imported as computer-aided designs (CAD) in STL-file format to the user software Think3D (UpNano GmbH). The tensile specimen T1 was designed as specified in the standard ISO 527-2 (2012) (Specimen 5B)[75] using NX 12 CAD software (Siemens, Germany). Specimen T2 was scaled down from T1 by reducing the dimensions of the narrow parallel part by a factor of 2 (**Table 2**; and Figure S36, Supporting Information). The microcuboids as well as the 3-point bending specimens B4 and B10 were designed directly in Think3D using the parametric cube element. Each microcuboid had a lateral length of 50 µm and a height of 80 µm. B4 and B10 stand for reduced dimensions of the preferred specimen given in ISO 178,[84] by a factor of 4 or 10, respectively, i.e., B4 has the dimensions 20 mm × 2.5 mm × 1 mm, B10 has the dimensions 8 mm × 1 mm × 0.4 mm (Figure S37, Supporting Information). All tensile and bending specimens were printed in batches of at least 6 pieces to ensure statistical relevance. Macrohardness test specimens with dimensions of 20 mm × 20 mm × 4 mm (Figure S39, Supporting Information) were printed using a 5x objective at 350 mW. For development, printed specimens were washed in isopropyl alcohol (IPA) twice and then removed from the substrate using a razor blade, whereas the microcuboids were directly analyzed on the glass substrates after development. To investigate postcuring effects of 2PP fabricated specimens the samples were UV-cured following the protocol described in Section 2.2.2.

Table 1. Fabrication parameters and objectives used for the 2PP printed test specimens. If not otherwise stated, the specimens were tested after development without any postcuring treatment. For each parameter setting, at least six samples were fabricated.

Printing parameters	40×	10×	5×
Scanning speed [mm s^{-1}]	50, 100, 150	600	750
Mode	fine	coarse	coarse
d_{xy} [µm]	0.17	4	8
d_z [µm]	0.3	5	10
Laser power [mW]	4.9–12.9	60–140	150–350
Power step [mW]	1.6	20	50
Specimen type	Microcuboids, microtensile [9.7 mW]	T2, B10	T1, T2, B4, B10

Table 2. Printed volumes and fabrication times per macroscopic specimen for tensile and 3-point bending specimens using 5× or 10× objectives. Each batch of tensile and bending specimens consisted of at least 6 specimens. Macro hardness specimens were printed once.

Geometry	T1	T2	B4	B10	Hardness
Dimensions of one specimen (see also Figure 2; and Supporting Information)	5B acc. ISO 527-2 thickness 1 mm	Reduced parallel part of 5B: 6×1×0.5 mm^3	20×2.5×1 mm^3	8×1×0.4 mm^3	20×20×4 mm^3
Volume [mm^3]	150	60	50	3.2	1600
Time using 10× [min]	–	221	–	11.7	–
Time using 5× [min]	88	61	26	2.4	850

2.2.2. UV-Curing of Reference Samples

For UV-polymerized reference samples (T1, T2, B4, B10), the UV-versions of the respective photopolymers were filled in a silicon mold. Air bubbles enclosed in the material were removed using a pipette. UV-curing was performed in two steps. The samples were first polymerized in a UV-flashlight-chamber with a rectangular shape (NK-OPTIK 280 N_2-box), equipped with two light sources (100 W each) with a spectrum of 280–700 nm (maximum between 400 and 500 nm). The flashlight frequency was 10 flashes s^{-1}. Curing was performed in N_2-Atmosphere with 1000 flashes. The samples were then demolded, turned, and cured again with 1000 flashes on the other side. To ensure complete curing, the sample-specimens were then illuminated in an Intelli-Ray 600 UV chamber (Uvitron, MA) for 5 min on each side at the maximum intensity of 600 W. A metal halide lamp (600 W) with a spectrum of 250–675 nm (maximum between 315 and 400 nm) was used as light source. After curing, the samples were finished with 800-grit sandpaper using an Ecomet V polishing and grinding machine (Buehler, Germany).

2.2.3. LCD 3D Printing

Liquid crystal display (LCD) 3D printing reference samples were produced from the UV-reference resins using a Photon Mono X LCD 3D printer from Anycubic (Shenzhen, China). The print jobs were created using the software Lychee Slicer (Vers. 5.4.3) (Mango3D, France). The following print settings were used: layer thickness 50 µm, exposure time 12 s, off time 2 s, bottom exposure time 60 s, bottom layers 5, Z lift distance 5 mm, Z lift speed 0.83 mm s^{-1}, Z retract speed 3 mm s^{-1}. All specimens were printed upright oriented. Half of the specimens were tested in green state within a week after printing, while the other half was postcured for 30 min at 60 °C using a Form Cure UV oven (Formlabs Inc.) before testing.

2.2.4. Stereolithography

Commercial reference specimens were printed on a Form 3 stereolithography printer from Formlabs Inc. (MA) using Clear Resin V4. The specimen-STL-files were uploaded to the operating software Preform (Ver. 3.31.0), oriented upright and support structures were created automatically using the One-Click Print feature. Layer spacing was set to Adaptive mode and Default v2.1 print settings were used. Half of the specimens were tested in green state within a week after printing, while the other half was postcured for 30 min at 60 °C using a Form Cure UV oven (Formlabs Inc.) before testing.

2.3. Voxel Line Measurements

Free hanging voxel lines were polymerized between printed walls using the 5× / 0.25 NA and 10× / 0.4 NA objectives in fine and coarse mode. Samples on borosilicate glass substrates were gold sputtered (Cressington sputter coater 108 auto), then mounted onto SEM stub holders (0°, 45°) using Carbon conductive tabs (PELCO Tabs, Ted Pella) and imaged with a Hitachi FlexSEM 1000 using the SE detector. The lines were measured directly from top view (lateral size) and at a 45° angle for side view. The axial voxel dimensions were calculated by multiplying the measured height with $\sqrt{2}$ (Pythagoras' theorem).

2.4. Surface Characterization

Scanning electron microscopy (SEM) was performed using Zeiss EVO 10 and Sigma 500 in high-vacuum mode. Fracture surfaces were gold-sputtered prior to observation. The double bond conversion was analyzed by infrared spectroscopy using an ATR-FTIR Bruker Tensor 27 equipped with a SensIR DuraSamplIR II ATR unit at a resolution of 4 cm^{-1}. Every spectrum was averaged from four measurements, two in parallel and two in the perpendicular orientation of the y-z-plane to the beam path, while every measurement was averaged from 32 single scans. After normalization with the help of the carbonyl peak at 1720 cm^{-1} the amplitudes A of the peaks around 810 cm^{-1} were used for calculating the double bond conversion DC by $DC = 1 - A_p / A_m$, whereas the indices m and p refer to the unpolymerized and polymerized state. Micro-ATR was conducted using a Bruker Hyperion 2000 FTIR microscope coupled to the Bruker Tensor 27 FTIR-spectrometer.

2.5. X-Ray Computed Tomography

The X-ray microscopes ZEISS Xradia 620 Versa at a resolution of 370 nm and ZEISS Xradia 810 Ultra at a resolution of 128 nm were used for volumetric imaging of parts of the macroscopic specimens to evaluate the homogeneity in the submicrometer

range. For NanoCT-imaging a parallel beam with a quasi-monochromatic energy of 5.4 kV was used to examine the samples. The 180° tomography was performed with 901 projections, each with an exposure time of 20 s per projection. Utilizing the large field of view objective resulted in a pixel size of 128 nm with a field of view of 64×64 µm^2 in the case of Xradia 810 Ultra. 360°-microCT (Xradia 620 Versa) was done with cone beam at 40 kV, 20 s exposure time and 801 projections. Here, the pixel size was 370 nm and the field of view 370×370 µm^2.

2.6. Microtensile Tests

In situ microscale uniaxial tension experiments were conducted with a custom nanoindentation setup inside a scanning electron microscope (InSEM, Nanomechanics Inc.; FEI Quanta 200F) on dog bone specimens printed with rectangular gauge sections of dimensions $50 \times 10 \times 7.5$ µm^3. Using a nominal strain rate of 10^{-3} s^{-1}, the specimens were strained to fracture unless precluded by severe postyield deformation outside the gauge section, in which case the tests would be terminated after load drops indicative of slipping or failure of the specimen grip. Frames of the in situ videos were analyzed with ImageJ to determine the proportion of deformation within the gauge section relative to the total measured extension. The corrected deformation as well as the raw load measurement were converted to engineering strains and stresses using the initial length (50 µm) and cross-sectional area of the gauge section. Then, the Young's modulus was estimated as the slope of the linear regime.

2.7. Macroscopic Mechanical Testing Methods

The strain rate for determining Young's modulus was 1% min^{-1} for tensile and bending tests and increased after that region. Different force sensors were used on a Zwick/Roell Z050 to best capture the applied loads and the applied loading devices, i.e., 2.5 kN for T1, 100 N for T2, and 20 N for bending tests. The sizes of the test specimens are given in Table 2 and Figures S36–S38, (Supporting Information). Prior to the measurements, each specimen was examined for defects such as enclosed air or cracks caused by shrinkage or poor handling, and sorted out if necessary. Only specimens that were broken in the test area were considered for data analysis.

2.7.1. Tensile Tests

T1 specimens were tested with standard parallel screw grips. T2 specimens were tested with custom-made clamps that combine form fit and parallel screw clamping. Tensile strain measurements were performed with the help of digital image correlation (DIC). Therefore, a speckle pattern was applied on the specimen's surface by spraying it with acrylic paint (Adler GmbH, Austria). The specimens were filmed with an EOS 700D camera (Canon, Japan) equipped with a macro-objective (Canon EF 100 mm f/2.8L Macro IS USM). Postprocessing of the recorded movies was performed with Adobe Premiere Pro and ImageJ.[86] Data were analyzed with NCorr[86] and NCorr post, Excel, and Origin Pro.

2.7.2. Bending Tests

The flexural testing tools were proportionally reduced regarding the dimensions given in ISO 178.[84] For example, the support span was 16 and 6.4 mm, and the support radii and the radii of the related loading edges were 1.25 and 0.5 mm for B4 and B10, respectively.

2.7.3. Dynamic-Mechanical Thermal Analysis

Dynamic-mechanical thermal analysis (DMTA) was performed on a TA Instruments DMA Q850 (Waters) in three-point bending mode with a dynamic strain amplitude of 0.05%. The ratio between static and dynamic load was 1.25. A standard 10 mm and a custom-built 6.4 mm support span were used for specimen sizes B4 and B10, respectively. Also, short-time creep tests were carried out on this DMTA device. The specimens were loaded at 5 MPa and held for 10 h.

2.7.4. Notch Sensitivity

Notch sensitivity was evaluated in 3-point bending mode on specimen geometry B4 (thickness B = 1 mm, width W = 2.5 mm), produced with a rectangular notch (depth a = 0.5 mm and width b = 0.2 mm, Figure S38, Supporting Information) at 350 mW. A span width s of 10 mm was used at a Zwick/Roell Z050 testing machine equipped with a 100 N load cell.

2.7.5. Hardness Measurements

The microhardness of the polished cross-sections and the microcuboids were measured using a nanoindentation device (Hysitron TI 750L Ubi, Bruker) in load-controlled mode. Loading time was 20 s, followed by a holding time of 30 s at maximum load and an unloading time of 10 s. Shore D hardness (ISO 868)[76] was determined with a Hildebrand durometer fixed in a stativ, ball indentation hardness measurements (ISO 2039)[77] were performed on a Kögel HPK 4/20B. In both cases, the specimens had dimensions of 20 mm × 20 mm × 4 mm (Figure S39, Supporting Information).

2.7.6. Density

The density of 2PP fabricated B4 specimens (laser power 350 mW) was determined by buoyancy method with a Sartorius BP211D analytical balance using a density determination kit.

3. Results and Discussion

3.1. Fabrication of Specimens by 2PP

Three different acrylate-based 2PP photopolymer materials were thoroughly investigated. Two of these resins have been developed with upscaled 2PP in mind and are commercially available (UpPhoto,[63,67,87,88] UpDraft), whereas the third one is a

custom mixture of triacrylates (ETA/TTA) frequently used in 2PP studies.[14,66,79,89–91] The commercial materials are based on a mixture of mono-, di-, and trifunctional acrylate monomers and oligomers with aliphatic and ethoxylated backbone (UpPhoto) or a mixture of di- and trifunctional acrylate monomers and oligomers with aliphatic and polyester backbone (UpDraft). In contrast to ETA-TTA, which is highly-crosslinked and thus more brittle consisting of a mixture of two triacrylates, UpPhoto, and UpDraft also contain urethane functional groups (**Figure 3**b; and Figure S3, Supporting Information). Urethans increase the toughness of brittle, highly-crosslinked (meth)acrylate photopolymers by adding noncovalent intermolecular hydrogen bonds between urethans and other functional groups, such as esters and ethers.[92–95]

Specimens were fabricated using three different objectives (5×, 10×, 40×) with distinctively different voxel sizes (Figure 1c; and Figures S1 and S2, Supporting Information) and consequently required different printing parameters for fabrication. Various printing parameters and specimen sizes were comprehensively tested with the different objectives. The dimensions of the specimens, as well as the printing parameters and resulting built times of a specimen for the different objectives, are shown in Tables 1 and 2. All macroscopic specimens were fabricated in vat mode using the proprietary adaptive resolution coarse mode, optimized for fast production (Figure 2).[64-67] Individual specimens were printed at constant power without using any special method to improve surface roughness or generate a gradient behavior. Also, the orientation of the scanning direction to the applied loading direction during the different test methods was chosen unfavorable, i.e., scanning the laser along the *x*-axis but applying the load during material characterization perpendicular to the xy-plane. These two constraints ensure that the observed mechanical behavior and the measured values represent the lower limit, especially regarding strength and toughness. If not otherwise stated, no postcuring was applied, and the specimens were measured directly as printed.

3.2. Basic Characterization

To check the performance and process window on the microscale, a set of microcuboids ($50 \times 50 \times 80\ \mu m^3$, Table 1) were printed using a 40× objective (NA 1.4). Cuboids are a typical geometry for fast screening of processing parameters.[14] While often only the shape or general appearance is evaluated, mechanical properties can also be tested. The focus here was laid on applying reasonable high scanning speeds (50–150 mm s^{-1}), and the quality was evaluated by both the appearance and indentation hardness of the resulting cuboids. Figure 3a; and Figures S4–S6, (Supporting Information) show the results of the nanoindentation measurements. While the indentation hardness does vary significantly for ETA/TTA (Figure 3a; and Figure S6, Supporting Information), it is relatively constant for UpDraft (Figure 3a; and Figure S5, Supporting Information) and UpPhoto (Figure 3a; and S4, Supporting Information). The lowest hardness values in the observed processing range are only 11% and 23% lower than the maximum values for UpPhoto and UpDraft, respectively, and occur at low energies and high scanning speeds. These results indicate a good dynamic range, i.e., processing window, of these two materials. In the case of ETA/TTA, it was not possible to achieve proper cuboids at 4.9 mW and 100 and 150 mm s^{-1}, and the dependency of hardness on the processing conditions is higher. Interestingly, there seems to be an optimum hardness at medium laser powers for ETA/TTA.

Figure 3b–d shows the results of a basic characterization of macroscopic samples fabricated using the 5x objective at a power of 350 mW. A SEM analysis of cryo-fractured surfaces of B4 specimens revealed that the parts were dense, without pores or fabrication-caused inhomogeneities for UpDraft and UpPhoto, whereas sub 400 nm irregularities are visible at the voxel line interfaces for ETA/TTA (Figures S7c, S8c and S9c, Supporting Information). B10 specimens from ETA/TTA printed with the 10× objective show also such irregularities that are about 100 nm in size but randomly distributed (Figure S11, Supporting Information). It is not clear where these come from, maybe from segregation. In the case of UpPhoto the cryo-fractured surfaces show parabola like structures which could result from the influence of segregations on the crack growth even in the cryo-cooled state (Figures S14 and S15, Supporting Information). Occasionally, large bubbles up to 70 µm are also visible at the ETA/TTA T2 fracture surfaces (Figure S16, Supporting Information). The presence of these irregularities does not seem to influence the cryo-fracture surface formation. Furthermore, and most important, there was no indication that the stitching areas or block overlaps had an impact on the formation of the fracture surfaces. The fracture surfaces are comparable to those typical for brittle polymers, not following stitching areas (Figures S7–S16, Supporting Information). Sub-µm X-ray microscopy also revealed good homogeneity in the examined volume with the exception of some larger inclusions of unknown origin in the examined UpPhoto volume (Figures S17 and S18, Supporting Information). Microhardness measurements across the xy-plane of polished cross-sections demonstrated the absence of significant gradients of indentation moduli along the entire specimen cross-section (Figure 3d). However, a slight reduction of modulus near the edge of the sample could be observed. This effect can be explained by the diffusion of inhibiting oxygen. In the course of polymerization, dissolved oxygen is consumed and oxygen from the surrounding unpolymerized resin diffuses through the edges of the structure. However, due to the larger diffusion distance to the center of the FoV, the oxygen concentration is diminished there, resulting in a higher relative polymerization efficiency and thus cross-linking density than at the edges of the structure.[96,97] The absolute numbers of indentation modulus are somewhat higher (UpPhoto, UpDraft) and somewhat lower (ETA/TTA) compared to the values obtained by indentation testing of microcuboids (Figures S4–S6, Supporting Information), but in the same range. This indicates a comparable degree of cross-linking at this different size-scales (micro and macro) and processing conditions (40× / 1.4 NA vs. 5× / 0.25 NA).

A double bond conversion between 89% and 96% for 2PP produced specimens (B4, 350 mW) can be calculated from ATR-FTIR (Figure 3b). A more detailed view of the FTIR spectra is given in Figure S3, (Supporting Information). Additionally, results from micro-ATR-FTIR are presented in Figures S19 and S20 (Supporting Information), showing the same double-bond conversion in the B4 and B10 specimens fabricated with 5× and 10× objective, respectively, and a lower double-bond conversion in the

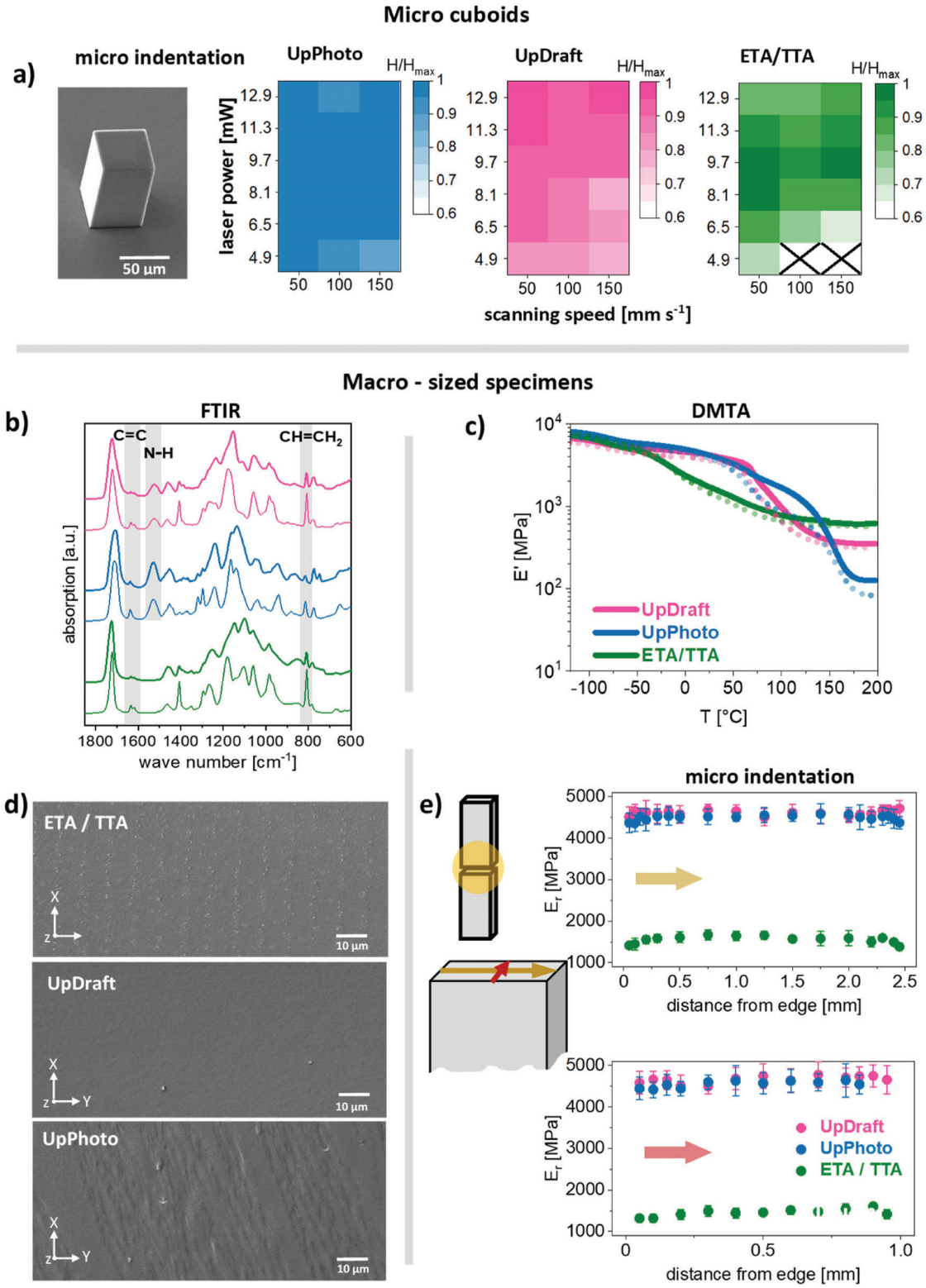

Figure 3. Basic characterization of 2PP printed specimens: a) Microcuboids were fabricated using the 40× / NA 1.4 objective to measure the relative indentation hardness in dependence on the processing conditions. Macroscopic bending specimens: b) FTIR-spectra of the uncured resin (thin lines) and 2PP processed photopolymers (thick lines). c) DMTA: storage modulus *E'* versus temperature of macroscopic 2PP specimens (full lines) compared to UV-casted reference specimens of the same base resins (dotted lines). *E'* is slightly higher for 2PP samples compared to UV-cured specimens. d) SEM images of cryo-fractured cross-sections of 2PP fabricated macroscopic bending specimens showing a dense morphology. e) Indentation modulus from nanoindentation on polished cross-sections of 2PP fabricated macroscopic bending specimens in thickness (top) and width direction (bottom).

micro tensile specimens fabricated with 40×. A gradient of double bond conversion over the cross-section with lower values in the edge region was detected, which tends to follow the trend of the microhardness results. Besides the already mentioned differences in oxygen concentration also variations of chain orientation at the free surfaces can influence the double-bond conversion. Dynamic mechanical analysis (DMTA) was used to compare 2PP specimens to UV-cured reference specimens of the same base resins (Figure 3c). Interestingly, DMTA revealed that the temperature dependencies of the storage moduli *E'* show higher values for 2PP fabricated samples when compared to UV-cured samples, indicating a higher cross-linking density for 2PP samples. The general visco-elastic behavior varies significantly between the materials. A more detailed view of the behavior of the moduli and damping can be found in the Supporting Information (Figures S21–S23, Supporting Information). The observed differences in thermo-mechanical behavior need to be considered for applications at the respective temperatures.

3.3. Tensile Testing

Next, the effect of various production parameters and possible size effects on the tensile properties were examined. T2 samples were fabricated using the 10× and 5× objective, while T1 were produced with the 5x only due to the larger volume and hence significantly longer built time (Table 2). For comparison, tests on microsized tensile specimens fabricated with the 40× objective were carried out (**Figure** 4a). It is obvious that the microspecimens reach larger elongation at break and maximum stresses, whereas the modulus and strength according to ISO 527-1 is comparable for UpDraft and UpPhoto at the investigated sizes. The higher elongation at break should be the well-known effect of statistically reduced occurrence of imperfections in small volumes in combination with an expectable higher homogeneity when printing with higher magnification objectives and lower scanning speeds. In the case of ETA/TTA, a softening was observed on the microscale, following the trend observed for ETA-TTA micro cuboids, which show a larger dependency on printing conditions. Furthermore, the dependency on the double-bond conversion seems to be higher in case of ETA/TTA. In general, it should be noted that the strain rate was lower in the microtests after the modulus region, i.e., at strains >0.25%, and the double-bond conversion was also lower in the microtensile specimens. This could be a further reason for a higher elongation at break but, not for such a large difference. The stress–strain curves of the macroscopic specimens of all tested materials and parameters, including UV-cured samples as reference, can be found in Figure S24, (Supporting Information). The material properties of ETA/TTA showed a high dependency on the objective and fabrication parameters. While it was possible to fabricate T2 samples from ETA/TTA using the 10× objective at various power settings, tensile specimens fabricated with the 5× objective at laser powers below 300 mW exhibited tension cracks. Consequently, it was only possible to produce T1 samples from ETA/TTA at 300 and 350 mW using the 5× objective. T1 samples fabricated at lower powers, and all of the thinner T2 samples either broke during the printing process or in course of development, or had pronounced cracks and defects. 2PP photopolymers with a high-crosslinker content such as ETA/TTA are typically designed to manufacture microscopic free-standing structures using high NA objectives.[53,98] However, when up-scaling such materials, extensive shrinkage stress can occur due to the high crosslinking density and resulting brittleness, leading to warpage or even cracking of the part. Looking at the fracture surfaces of T1 and T2 specimens it stands out that the surfaces of UpDraft and UpPhoto are much more rugged than the very smooth surfaces of ETA/TTA (Figure 4b; and Figures S7–S9, S26–S28, Supporting Information). This should be an indication for more energy dissipation during fracture of these two materials. Nevertheless, there is no indication of plasticity visible, which is not surprising for highly cross-linked materials.

Notably, 2PP specimens produced at higher powers showed comparable mechanical behavior to UV-cured reference specimens immediately after printing, without the need for postcuring. The stress–strain curves of the T2 specimens (10x) of all resins show a dependency on the fabrication power, indicating that samples produced at higher powers were more brittle but had a higher tensile strength. However, the strength was comparable between T1 and T2 specimens. In contrast, the UV-cured samples showed a lower strength for the larger T1 specimens. This difference is most likely caused by the different fabrication approaches leading to a higher number of defects in the UV-cured T1 samples, indicating that 2PP allows the production of relatively homogenous samples.

Figure 4c shows the Young's moduli of all tested materials and parameter settings. The Young's moduli are increased for T2 specimens compared to T1 for all materials and fabrication powers. However, the magnification of the objective has no impact on the Young's moduli of the T2 samples. The Young's moduli of UpDraft and UpPhoto do not vary significantly with the fabrication power. In the case of the T1 specimens fabricated using the 5× objective, the values are constant, while a small step occurs for the T2 specimens when the laser peak intensity is increased from 600 to 800 GW cm^{-2} before reaching a plateau. An increase in the Young's moduli with fabrication power can be observed for T2 specimens produced with ETA/TTA. A dependency of the mechanical properties of 2PP specimens on the structuring parameters was already previously reported for acrylate-based resins.[34,53,57] In those studies, it was shown that key parameters, such as writing speed and layer- and line-spacing impact the mechanical properties and influence the double bond conversion. Increased power resulted in a higher double bond conversion and higher Young's moduli, indicating the formation of a stronger polymer network. The moduli of the 2PP printed macroscopic specimens from UpDraft and UpPhoto reach the values of UV-casted specimens and the 2PP microtensile specimens. In the case of ETA/TTA, it can be seen that the modulus of elasticity of the microspecimens is lower than that of the macroscopic specimens.

3.4. 3-Point Bending Testing

Figure 5 shows the results of the 3-point bending tests for B4 and B10 specimens. Under 3-point bend loading, the influence of the processing conditions on the materials' stiffness is small,

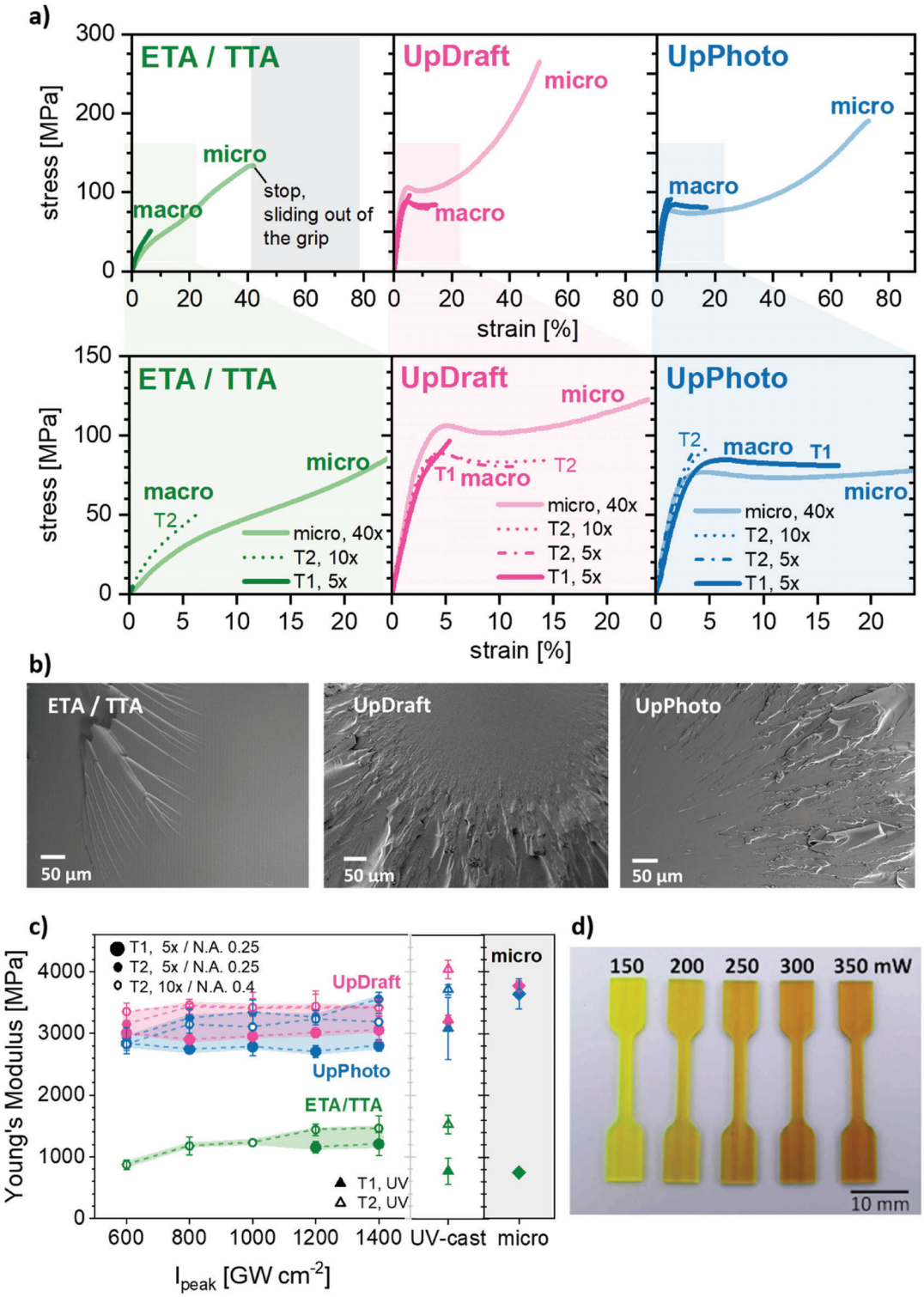

Figure 4. Tensile testing: a) Stress–strain curves of the microscopic (40×, 9.7 mW) and macroscopic (5×, 350 mW; 10×, 140 mW) 2PP fabricated specimens show comparable stiffness and strength behavior but strongly different elongation and stress at break for UpDraft and UpPhoto. The strength of ETA/TTA in the case of T1 (5×) is extremely low due to occurring shrinkage cracks. A more detailed view on the tensile behavior of the macroscopic specimens can be found in Figure S24 (Supporting Information). b) SEM images of fracture surfaces of tested T1 specimens. The transition region from the initiation region to crack growth indicates stronger rugged surfaces of UpDraft and UpPhoto compared to ETA/TTA. c) Young's moduli of all tested sample variations and power settings. UV-casted macroscopic and microscopic 2PP samples were tested for comparison. d) Image of T1 2PP specimens fabricated with UpPhoto using different power settings. Here, the sample color became darker with increasing fabrication power, which was not the case for UpDraft and ETA/TTA.

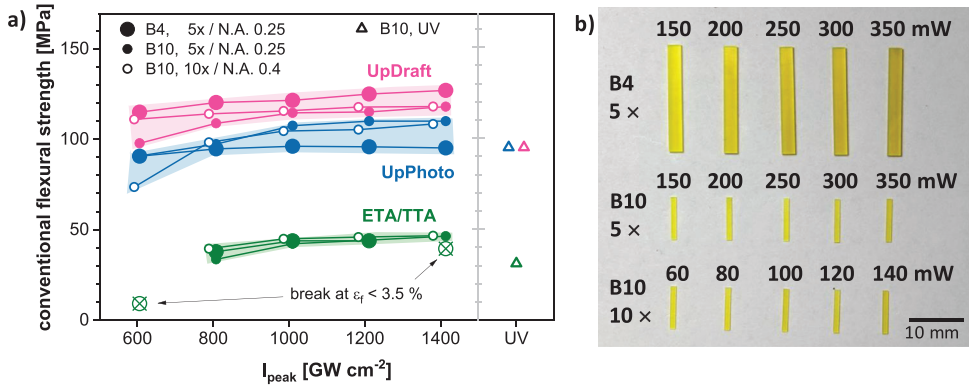

Figure 5. 3-Point bending tests. Test results of B4 and B10 specimens show the influence of the laser intensity and objective used for 2PP fabrication. a) Conventional flexural strength at 3.5% strain according to ISO 178 versus fabrication laser intensity. Depending on the objective and the fabrication power UpDraft and UpPhoto exhibit opposing behavior regarding the flexural strength. ETA/TTA has less favorable properties than the other two materials but shows a slightly broader processing window than observed in the tensile tests. In the case of B10 specimens, only the lowest fabrication powers (10×: 60 mW; 5×: 150 mW) failed right after printing. However, due to bubbles and low cross-linking density at 150 mW, and microcracks resulting from internal stresses at 350 mW the strength drops dramatically for these two power settings limiting the working range of ETA/TTA from 200 to 300 mW. For all materials the 2PP B10 specimens fabricated at higher laser powers show higher strength than the respective UV-cured specimens. b) Exemplary image of B4 and B10 test specimens fabricated from UpPhoto.

and differences are more pronounced in the higher-loaded region. The flexural stress plotted against the flexural strain for all tested specimens can be found in (Figure S29, Supporting Information). Figure 5a shows the measured flexural strength of all tested materials and parameter settings. Interestingly, UpDraft and UpPhoto exhibit opposing behavior. Samples printed with the 10× objective from UpDraft show no dependence of flexural strength on fabrication power in the investigated range but a clearly visible dependence when printed with the 5× objective. Here, the strength increases with higher laser power. In contrast, in the case of UpPhoto, the fabrication power dependency was highest for samples printed with the 10x objective and specimen size B10. As observed in tensile testing, ETA/TTA has less favorable properties than the other two materials. However, the processing window is slightly broader than for the tensile specimens of the same material.

All the results presented so far (FTIR, DMA, tensile, and bending behavior) indicate a high double bond conversion of specimens fabricated with 2PP immediately after printing, without the need for postcuring. Next, the possibilities of modifying the properties by postcuring were investigated. Therefore, B10 bending specimens were exposed to thermal treatment (1 h at 160 °C) or UV irradiation. Practically no influence on the maximum bending stress, but an indication of a slight softening effect in the postcured samples at higher loads could be observed (**Figure 6**). This is possibly the result of entropy relaxation effects. For UpDraft, a relaxation peak in the DSC heating curve of the initial printed state is absent in the postcured state (Figure S30, Supporting Information). To evaluate possible aging effects and long-term stability of 2PP printed parts, a set of B10 samples was stored at room temperature for over a year in a polyethylene bag in the absence of light. Interestingly, no significant change in the bending behavior of UpPhoto and ETA/TTA could be observed after a year. In the case of UpDraft, a slight increase in stiffness and strength was measured (Figure 6; and Figure S31, Supporting Information).

Using the macrosized 2PP specimens B1, conducting short-time creep tests over several hours is now straightforward. In contrast, this is relatively difficult on the microscale due to often occurring long-time instabilities of microtesting devices due to thermal drift. In the case of macrosized specimens, these influences are negligible compared to the overall deformation. ETA/TTA shows more than two times higher values than UpPhoto and UpDraft at a creep compliance of 5 MPa bending stress (**Figure 7a**). This behavior could be expected due to the significantly lower stiffness of ETA/TTA. Overall, the creep compliance J and the creep modulus follow the order found for the modulus of elasticity, i.e., UpDraft shows the lowest creep compliance and the highest creep modulus. All compliance curves could be fitted by the simple exponential law defined by Findley,[99] $J(t) = J_0 + mt^n$, with the initial creep compliance J_0 and the constants m and n. The stress-independent Findley creep parameter n allows a very good differentiation of the materials (Figure 7b). Especially the results of UpDraft and UpPhoto highlight the importance of creep tests. While both materials perform comparably regarding stiffness and strength at room temperature, they show significant differences in their creep behavior, with UpDraft giving better performance. For short times it can be simplified that the product m*n determines the slope of the creep curve, which is lower for UpDraft. Looking back to Figure 3c, the stronger drop of storage modulus of UpPhoto compared to UpDraft in the room temperature region already indicated this behavior, which is a good representation of the time-temperature superposition rule. But it is obvious that with increasing time the exponent n dominates the behavior reflected by a beginning stronger drop of the creep modulus (Figure 7c).

In many applications 2PP fabricated parts are of complex geometries, e.g., containing notches. For this reason, knowledge about the influence of notches on the materials behavior is of importance. A relatively easy approach is the characterization of the so-called notch sensitivity. Mainly investigated for fatigue loading, it can also be determined for quasistatic loading.[100] As an

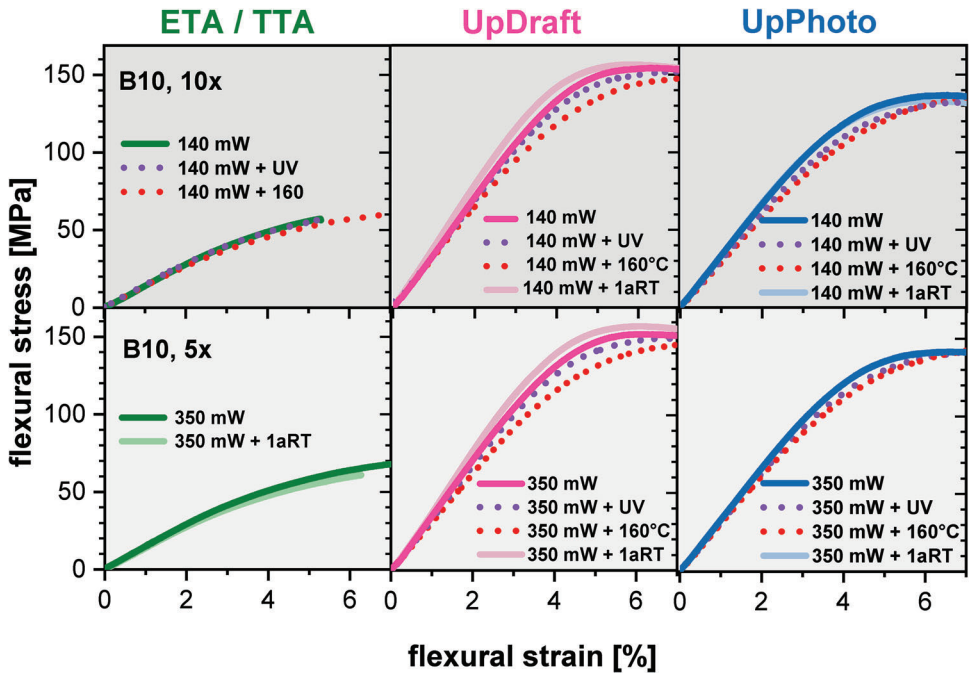

Figure 6. Effects of postcuring and aging. The influence of postcuring by thermal treatment (160 °C, 1 h), UV-radiation or long-term storage (>1 year at room temperature) of B10 specimens fabricated with the 5× or 10× objectives was investigated via the 3-point bending behavior. No significant change in the bending behavior was observed for UpPhoto and ETA/TTA, whereas UpDraft showed a slight variation in stiffness and strength after 1 year of aging.

often application driven test, it is a simple comparison between the performance of unnotched and notched specimens, often with varying notch types. An example is shown in **Figure 8**. Here, a B4 specimen with a rectangular notch was fabricated. Such a notch geometry can be found in microfluidic devices or casting molds. All of the investigated materials show brittle behavior in the notched state (Figure 8), but it is clearly visible that UpPhoto shows the lowest notch sensitivity of the three materials. The reduced stiffness results from the reduced cross-section in the notched area and is not taken into account. Interestingly, thermal treatment and, therefore, a homogenization of the polymer structure and internal stresses does not lead to an improvement. These results are of significant interest since many small-sized parts made by 2PP contain relatively sharp notches due to geometric restrictions or as a requirement for the intended application. Obviously, the results of such a test depend on the materials intrinsic properties, the printing process and the resulting quality of the bulk, the geometry of the notch and the fabrication strategy

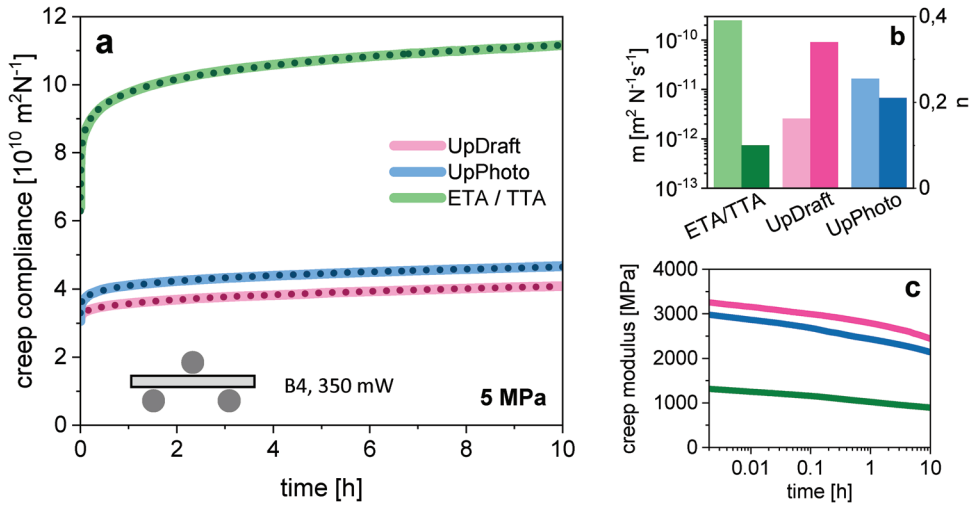

Figure 7. Short-time creep behavior under 5 MPa bending stress. a) Creep compliance versus time. The dotted lines represent the application of Findley's model. b) Creep parameter m (light) and n (dark) for the short-time behavior derived from the creep compliance curves and c) creep modulus.

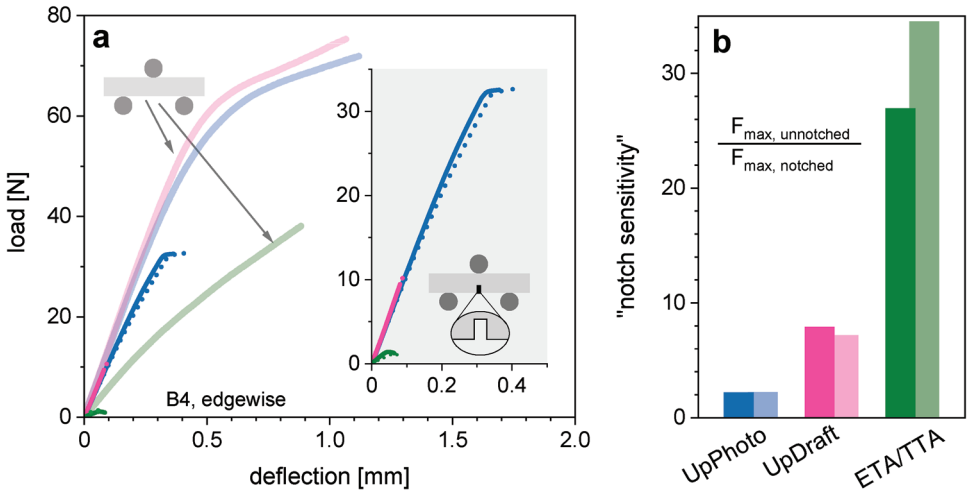

Figure 8. Notch sensitivity in 3-point bending mode with rectangular notch: a) Load-deflection curves of un-notched and notched B4 specimens, edgewise testing. b) "Notch sensitivity" as the ratio between maximum load of the unnotched to the notched state without taking into account the influence of stiffness reduction by reducing the cross-section area. The dotted lines and the light bars represent thermally annealed (1 h at 160 °C) samples.

of the notch. To exclude the influence of the printed notch and to get a more general statement about a 2PP printed material, also B4 specimens with a cut notch were analyzed, which offers the possibility to apply fracture mechanics testing and to compare the obtained values with values of molded bulk specimens (Figure S32, Supporting Information). In a first approach, short notches of 120 µm have been introduced in the best performing material UpPhoto by razor blade cutting in B4 specimens resulting in a very short crack length a to width W ratio (a/W) of 0.045. If one ignores the typical requirements for a larger (a/W) ratio and calculates approximately the fracture toughness K_{Ic}, a value of about 1.3 MPam$^{1/2}$ can be obtained, which is in a range with epoxy,[101] PS,[102] PMMA,[103] porcelain, or MgF. In literature,[104] a K_{Ic} 0f 0.57 MPam$^{1/2}$ was found for microsized 2PP specimens with a sharp, printed notch made of IP-Dip (Nanoscribe), a widely used commercial acrylate-based 2PP photopolymer.

3.5. Macroscopic Indentation Hardness Tests

Even specimens suitable for macrohardness testing are now accessible with suitable 2PP photopolymers and high-throughput 2PP systems. **Figure 9** shows an example of large-scale specimens having the dimensions 20 mm × 20 mm × 4 mm, fulfilling the requirements for ball indentation hardness testing [ISO 2039-1:2001] and Shore D testing [ISO 868:2003]. Despite their simple rectangular shape, fabricating such specimens by 2PP is quite challenging due to the large bulk volume. It was not possible to build specimens of this dimension from ETA/TTA due to massive shrinkage-induced deformation and cracking. Moreover, the fabrication time should be minimized because only one (or two, if both sides of the plate are used) measurement can be done on a plate of this geometry to meet the criteria given in the standards for minimum distances from the edges. The test results are listed in **Table 3**.

3.6. Comparison of 2PP to Other Additive Manufacturing Technologies

As demonstrated so far, no postcuring is obviously required for the 2PP materials investigated, since parts possess their full mechanical properties right after printing. This is a significant advantage over other resin-based 3D printing technologies (DLP, SLA, LCD), which only deliver green parts and thus require postcuring, as even fragile geometries can be cleaned in solvents

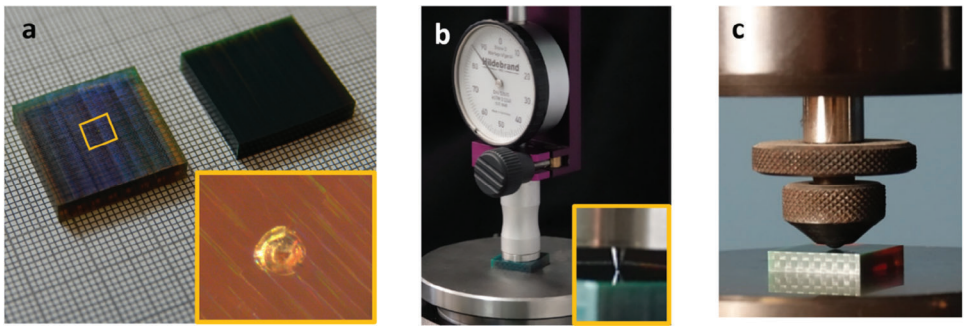

Figure 9. Hardness tests. a) 2PP-printed specimens (20 × 20 × 4 mm^3) appropriate for macrohardness testing from UpPhoto and UpDraft and a resulting Shore D indent (inset). b) Shore D testing according to ISO 868 and c) ball indentation testing according to ISO 2039.

Table 3. Summary of the tested material characteristics determined on 2PP printed macroscopic specimens made from UpPhoto, UpDraft, and ETA/TTA using the 5× objective (NA 0.25) at 350 mW or the 10× objective (NA 0.4) at 140 mW. Microtensile specimens (TM) have been fabricated using the 40× objective (NA 1.4) at a laser power of 9.7 mW.

	UpPhoto				UpDraft				ETA/TTA			
Density [g cm^{-3}]	1.21				1.22				1.235			
	Tensile tests											
	T1 5x	T2 5×	T2 10×	TM 40×	T1 5×	T2 5×	T2 10×	TM 40×	T1 5×	T2 5×	T2 10×	TM 40×
Young's Modulus [GPa]	2.8	3.5	3.2	3.6	3.1	3.4	3.4	3.7	1.2	–	1.5	0.73
Tensile strength [MPa]	85	95	90	77	80	89	92	107	4	–	51	–
Elongation at break [%]	12	18	6	74	4	10	12	49	0.4	–	8	(> 40)
	Bending tests											
	B4 5x	B10 5×	B10 10×	B4 5×	B10 5×	B10 10×	B4 5×	B10 5×	B10 10×			
Conventional flexural strength at 3.5% strain[a] [MPa]	95	110	108	127	118	118	44	46	47			
Maximum calculated stress during the test[b] [MPa]	132	142	137	158	148	147	63	66	69			
	Hardness tests											
Shore D	85			86			–					
Ball Indentation hardness [N mm^{-2}]	174			181			–					
	Dynamic – mechanical thermal analysis (1 Hz)											
E' at 23 °C [MPa]	4100			4240			1750					
E' at 37 °C [MPa]	3590			4140			1480					
E' at 80 °C [MPa]	2080			1770			850					
E' at 120 °C [MPa]	1150			570			600					

[a] According to ISO 178; [b] Taken from the load maximum, calculated without correction for large deflections.

without special care. For example, for the production and subsequent postprocessing of delicate structures, complex parts, and microfluidic devices that have overall dimensions in the mm or even cm range, but contain thin (<100 µm), long channels (>1 mm) that require extended development time in solvent or even the use of pumps to flush such microchannels, a high degree of cure right after printing is essential.[64,66,67] With a technology that only provides semicured green parts, such conditions might result in swelling or even fracture of the part, while postcuring by UV or heat is not applicable before microchannels and cavities are cleared to avoid clogging. To illustrate the typical UV-based 3D printing process, we have printed the same set of specimens (T1, B4) using a commercial Formlabs Form 3 platform with the Formlabs resin Clear V4 and the corresponding postcuring chamber Form Cure according the manufacturer's instructions. The different mechanical behavior between green parts and postcured parts is obvious (Figure S33, Supporting Information). When producing testing specimens directly by 2PP, the real mechanical properties of the 2PP resins can be accessed. The 2PP resin formulations usually differ from DLP or SLA resins as different photoinitiators are used and no light absorbers are necessary.[14] In addition, direct testing of 2PP printed specimens allows to evaluate the 2PP printing process itself, e.g., whether the chosen print settings yield parts with anticipated materials properties. A direct comparison with DLP or SLA printed specimens of the same base resin is not useful due to the necessary postcuring step. For comparison, we produced testing specimens (B4, B10, T1, T2) from UV-resins using an LCD-based 3D printer (Anycubic Photon X Mono, 405 nm) and an LED chamber for postcuring (Formlabs Form Cure). Since UV-based 3D printing produces green parts that need to be postcured, the results of the LCD specimens differ from those produced by 2PP (Figures S29 and S34, Supporting Information), most probably due to insufficient postcuring of the LCD 3D printed parts. However, for 2PP users, it is not necessary to take the detour via UV-based 3D printing with modified resins. The macroscopic specimens can be directly produced and the mechanical properties can be determined using conventional testing equipment.

When comparing 2PP to other high-resolution additive manufacturing technologies, high-throughput 2PP 3D printing, when using a material vat, resembles a CLIP process with an optical dead zone.[81] This is a great advantage over projection microstereolithography (PµSLA), as parts do not have to be delaminated from the bottom of the vat after every layer, which can damage fragile parts and adds a time delay of typically 4–5 s per layer.[105] However, it is reasonable to compare high-throughput

2PP to single-digit-micrometer-resolution CLIP, where an oxygen diffusion layer is used to inhibit polymerization at the bottom of the vat. Joseph M. DeSimone and co-workers have recently presented this high-resolution CLIP technology, claiming to achieve 10^5 times faster print speeds than a Nanoscribe 2PP system and 25–100 times faster print speeds than DLP and PμSL.[106] Within this paper they showcased printing of a twisted lattice bar design, which was produced using high-resolution CLIP as well as a Nanoscribe Photonics GT 2PP system equipped with a 25× objective using unspecified print settings. The structure is 20 mm high and seems to have a 5 × 5 mm^2 base area with a minimum feature size of 100 μm. The authors stated a print time of 1.5 h with their system, whereas the print with the Nanoscribe system was aborted after 200 μm height and 48 h of print time. Due to unavailability of the STL data set of the twisted lattice bar for direct comparison, we printed an octet truss structure with similar complexity using the NanoOne equipped with either the 5× or the 10× objective in coarse mode (Figure S35, Supporting Information). When using the 5×/NA 0.25 objective on the NanoOne, the octet truss bar could be printed within 2 h which is quite comparable to high-resolution CLIP[106] (when the 2× objective is used). With the 10× objective the dimensions of the structure were scaled down by a factor of 2. The size of the minimal feature was reduced to 50 and 25 μm, respectively. Both structures could be fabricated in 1.1 h independently of the minimum feature size, as galvo scanning was used. Consequently, the upscaled part (5 μm × 5 μm × 20 000 μm) with equal resolution would be printed with the 10× objective in ≈9 h.

In the case of high-resolution CLIP (equipped with a light engine with a 2560 × 1600 array of pixel), the twisted lattice bar seems to be written using a 2× objective with 3.8 μm pixels size. In contrast, the higher resolution 5× objective with 1.5 μm pixel size would require stitching, which was not possible with the presented setup. In comparison, the resolution tests in the same paper were conducted using the 5× objective. The print speed of the 5× objective is estimated to be 6.4 times slower than that of the 2× objective, if the same area is printed with the same z-layer height (pixel area (2×)/pixel area (5×) = 6.4). Hence, the print speed of high-resolution CLIP equipped with a 5x objective is comparable to a 10× 2PP print (≈9–10 h). Due to the low dead zone thickness of ≈3–5 μm in high-resolution CLIP, the print time is also highly dependent on the resin viscosity, which influences the time a resin requires to reflow after a layer has been polymerized and the stage has been moved. With 2PP, resin viscosity is not so critical as the optical dead zone can be set within the working distance of the objective (typically up to several 100 μm, in the case of the 5× even several mm). Moreover, for low NA objectives, a refractive index mismatch between the immersion medium and the resin is less critical for the voxel shape.[107,108] Consequently, the resolution in this case is less affected by depth-dependent optical aberrations. In general, high-throughput 2PP with low NA objectives is a quite versatile technology for a broad material portfolio.

4. Conclusion

For the first time, a wide range of mechanical properties, from classical mechanical tests, such as tensile, flexure, and hardness, to creep and even fracture behavior, was determined for 2PP processed materials on the macroscale. Additionally, the thermomechanical behavior of 2PP materials was also investigated. This is a crucial step to further establish 2PP as an additive manufacturing technology for industry and expand the field of applications of this technology. It could be shown that the new generation of commercially available 2PP 3D printers is capable of producing macroscopic testing specimens in the centimeter range at an acceptable built time using low NA objectives and 2PP resins that are processable at very high volumetric built rates of up to more than hundred $mm^3\ h^{-1}$ and that are therefore suitable for upscaling. Those are essential requirements to close the gap toward larger additive microfabrication technologies such as high-resolution CLIP,[108] micro-SLA,[109] and volumetric 3D printing.[110,111] Notably, all macroscopic mechanical characterization could be performed with standard testing devices. This is particularly useful for translating from a mostly lab-based (micro-)testing process of highly specialized facilities to a more conventional and standardized industrial environment. Additionally, investigating the fracture areas showed that the stitching, which is crucial for large-scale 2PP printing, is not creating any weak points in the test specimens. This indicates that the process of up-scaling 2PP did not negatively influence the mechanical properties of the created specimens.

Furthermore, the importance of the mechanical characterization of 2PP materials with specimens on various size scales was demonstrated since mechanical characteristics cannot simply be translated from the microscale to the macroscale. ETA/TTA, a material that had been widely used experimentally for generating microsized parts, turned out to be not suitable for high scanning speed rates and up-scaling to the macrosize range due to a comparable small process window, the occurrence of microcracks as a result of internal stresses, and generally its very low toughness. The small process window of ETA/TTA was already indicated during manufacturing of the microcuboids using the high resolution 40x objective. To develop and improve materials for upscaled 2PP, such as UpDraft and UpPhoto, and characterize their material performance using standardized methods on the meso- and macroscale is crucial. On the one hand, this is necessary due to the already discussed different mechanical material behavior when scaling up. On the other hand, methods to analyze the efficiency of 2PP resins are currently mainly based on threshold tests where printing parameters are used that often do not reflect real fabrication scenarios, as we have discussed recently.[14] Standardized material testing on all size scales helps to understand the true potential for the application of newly developed 2PP materials. Moreover, standardized characterization protocols are also necessary for evaluation and control of the manufacturing process stability. Considering the short time needed to produce a batch of six B10 samples (<15 min) and the fact that these samples can be immediately measured by flexure tests and DMTA, the macroscopic 2PP testing approach allows quality control not only of the material but also of the printing process and comparison of different systems of the same production model.

Comparing the three investigated materials (Table 3), ETA/TTA, UpDraft, and UpPhoto, it could be shown that only the latter two are suitable for upscaling due to their large processing window and well-balanced mechanical properties. The modulus of elasticity and the hardness are similar to microscale specimens fabricated using the high magnification 40×

objective at lower scanning speed but the same mean laser intensity. The properties of the 2PP produced macrosized specimens without postcuring are at the level of or even better than bulk UV-cured specimens made from the same base resins using a UV-photoinitiator. Further, it was shown that compared to other light-based 3D printing processes, 2PP has the advantage that highly cured and thus robust parts are received immediately after printing. Consequently, UV or thermal postcuring can be avoided. This is a unique feature and especially a great advantage for the removal of uncured resin from microchannels in complex 3D printed microfluidic devices.

The results of this work highlight the importance of optimized and, in the best case, standardized testing procedures for 2PP materials on the meso- and macroscale, and shows the potential that lies within upscaled 2PP enabled by a new generation of high-throughput 2PP devices. With the new generation of 2PP systems and materials, the gate is opened for the future development and manufacturing of reliable, commercial functional parts and devices using 2PP and the establishment of novel functional materials.[112] Based on the results of this work first applications of the investigated materials in the cm scale could already be realized.[64,66,67,88]

Supporting Information

Supporting Information is available from the Wiley Online Library or from the author.

Acknowledgements

F.C.-G. and M.L. contributed equally to this work. Veronika Biegler (TU Wien) is acknowledged for her support the preparation of UV-casted samples. Till Jarnot and Pablo Vazquez Conde (both UpNano GmbH) are acknowledged for their help with CAD design of the testing specimens. Peter Gruber and Josef Thalhammer (both UpNano GmbH) are gratefully acknowledged for fruitful discussions. This work was supported by the Vienna Business Agency (Grant No. 2864518). The authors acknowledge TU Wien Bibliothek for financial support through its Open Access Funding Programme. [Correction added on August 22, 2024, after first online publication: Table 3 and Figure 5 has been updated.]

Conflict of Interest

A.O. is a co-founder and CSO of UpNano GmbH, a TU Wien spin-off and the manufacturer of the NanoOne device used in parts of this study. A.O. is a co-inventor of a patent on a two-photon polymerization apparatus, which UpNano GmbH is licensing from TU Wien. M.L. is an employee of UpNano GmbH. The authors declare no other conflict of interest.

Data Availability Statement

The data that support the findings of this study are available from the corresponding author upon reasonable request.

Keywords

additive manufacturing, batch production, mechanical testing, two-photon polymerization, upscaling

Received: August 21, 2023
Revised: January 2, 2024
Published online: February 16, 2024

[1] M. Göppert-Mayer, *Ann. Phys.* **1931**, *401*, 273.
[2] S. Maruo, O. Nakamura, S. Kawata, *Opt. Lett.* **1997**, *22*, 132.
[3] J. Stampfl, A. Ovsianikov, R. Liska, *Multiphoton Lithography*, Wiley-VCH, Vienna **2016**, https://doi.org/10.1002/9783527682676.
[4] W. R. Zipfel, R. M. Williams, W. W. Webb, *Nat. Biotechnol.* **2003**, *21*, 1369.
[5] B. H. Cumpston, S. P. Ananthavel, S. Barlow, D. L. Dyer, J. E. Ehrlich, L. L. Erskine, A. A. Heikal, S. M. Kuebler, I.-Y. S. Lee, D. McCord-Maughon, J. Qin, H. Röckel, M. Rumi, X.-L. Wu, S. R. Marder, J. W. Perry, *Nature* **1999**, *398*, 51.
[6] J. R. Bumstead, J. J. Park, I. A. Rosen, A. W. Kraft, P. W. Wright, M. D. Reisman, D. C. Côté, J. P. Culver, *Neurophotonics* **2018**, *5*, 25001.
[7] S. Wang, Y. Yu, H. Liu, K. T. P. Lim, B. M. Srinivasan, Y. W. Zhang, J. K. W. Yang, *Nano Futures* **2018**, *2*, 025006.
[8] V. F. Paz, M. Emons, K. Obata, A. Ovsianikov, S. Peterhänsel, K. Frenner, C. Reinhardt, B. Chichkov, U. Morgner, W. Osten, *J. Laser Appl.* **2012**, *24*, 42004.
[9] J. Fischer, G. von Freymann, M. Wegener, *Adv. Mater.* **2010**, *22*, 3578.
[10] X. Zhou, Y. Hou, J. Lin, *AIP Adv.* **2015**, *5*, 030701.
[11] C. Arnoux, L. A. Pérez-Covarrubias, A. Khaldi, Q. Carlier, P. L. Baldeck, K. Heggarty, A. Banyasz, C. Monnereau, *Addit. Manuf.* **2022**, *49*, 102491.
[12] C. Arnoux, T. Konishi, E. Van Elslande, E.-A. Poutougnigni, J.-C. Mulatier, L. Khrouz, C. Bucher, E. Dumont, K. Kamada, C. Andraud, P. Baldeck, A. Banyasz, C. Monnereau, *Macromolecules* **2020**, *53*, 9264.
[13] P. Kiefer, V. Hahn, M. Nardi, L. Yang, E. Blasco, C. Barner-Kowollik, M. Wegener, *Adv. Opt. Mater.* **2020**, *8*, 2000895.
[14] M. Lunzer, J. S. Beckwith, F. Chalupa-Gantner, A. Rosspeintner, G. Licari, W. Steiger, C. Hametner, R. Liska, J. Fröhlich, E. Vauthey, A. Ovsianikov, B. Holzer, *Chem. Mater.* **2020**, *34*, 3042.
[15] G. Kumi, C. O. Yanez, K. D. Belfield, J. T. Fourkas, *Lab Chip* **2010**, *10*, 1057.
[16] B. W. Pearre, C. Michas, J. M. Tsang, T. J. Gardner, T. M. Otchy, *Addit. Manuf.* **2019**, *30*, 100887.
[17] A. Dobos, J. Van Hoorick, W. Steiger, P. Gruber, M. Markovic, O. G. Andriotis, A. Rohatschek, P. Dubruel, P. J. Thurner, S. Van Vlierberghe, S. Baudis, A. Ovsianikov, *Adv. Healthcare Mater.* **2019**, *9*, 1900752.
[18] J. Kato, N. Takeyasu, Y. Adachi, H.-B. Sun, S. Kawata, *Appl. Phys. Lett.* **2005**, *86*, 044102.
[19] S. Matsuo, S. Juodkazis, H. Misawa, *Appl. Phys. A* **2005**, *80*, 683.
[20] L. Kelemen, S. Valkai, P. Ormos, *Opt. Express* **2007**, *15*, 14488.
[21] M. Manousidaki, D. G. Papazoglou, M. Farsari, S. Tzortzakis, *Opt. Lett.* **2020**, *45*, 85.
[22] L. Yang, D. Qian, C. Xin, Z. Hu, S. Ji, D. Wu, Y. Hu, J. Li, W. Huang, J. Chu, *Opt. Lett.* **2017**, *42*, 743.
[23] V. Hahn, P. Kiefer, T. Frenzel, J. Qu, E. Blasco, C. Barner-Kowollik, M. Wegener, *Adv. Funct. Mater.* **2020**, *30*, 1907795.
[24] W. Chu, Y. Tan, P. Wang, J. Xu, W. Li, J. Qi, Y. Cheng, *Adv. Mater. Technol.* **2018**, *3*, 1700396.
[25] S. K. Saha, D. Wang, V. H. Nguyen, Y. Chang, J. S. Oakdale, S. C. Chen, *Science* **2019**, *366*, 105.
[26] W. Ouyang, X. Xu, W. Lu, N. Zhao, F. Han, S. Chen, *Nat. Commun.* **2023**, *14*, 1716.
[27] N. Hauptmann, J. Ludolph, H. Rothe, J. Rost, A. Krupp, J. Lechner, S. Kohlhaas, M. Winkler, B. Stender, G. Hildebrand, K. Liefeith, *Int. J. Mol. Sci.* **2022**, *23*, 3115.
[28] T. Tičkūnas, D. Paipulas, V. Purlys, *Opt. Mater. Express* **2020**, *10*, 1432.
[29] M. Luitz, M. Lunzer, A. Goralczyk, M. Mader, S. Bhagwat, A. Warmbold, D. Helmer, F. Kotz, B. E. Rapp, *Adv. Mater.* **2021**, *33*, 2101992.

[30] B. Lamprecht, A. Ulm, P. Lichtenegger, C. Leiner, W. Nemitz, C. Sommer, *Appl. Opt.* **2022**, *61*, 1863.
[31] Z. Bayindir, Y. Sun, M. J. Naughton, C. N. LaFratta, T. Baldacchini, J. T. Fourkas, J. Stewart, B. E. A. Saleh, M. C. Teich, *Appl. Phys. Lett.* **2005**, *86*, 64105.
[32] C. Y. Khripin, C. J. Brinker, B. Kaehr, *Soft Matter* **2010**, *6*, 2842.
[33] C.-S. Shin, T.-J. Li, C.-L. Lin, *Micromachines* **2018**, *9*, 615.
[34] J. Bauer, A. Guell Izard, Y. Zhang, T. Baldacchini, L. Valdevit, *Adv. Mater. Technol.* **2019**, *4*, 1900146.
[35] Y. Tao, C. Wei, J. Liu, C. Deng, S. Cai, W. Xiong, *Nanoscale* **2019**, *11*, 9176.
[36] N. Rohbeck, R. Ramachandramoorthy, D. Casari, P. Schürch, T. E. J. Edwards, L. Schilinsky, L. Philippe, J. Schwiedrzik, J. Michler, *Mater. Des.* **2020**, *195*, 108977.
[37] J. Bauer, A. G. Izard, Y. Zhang, T. Baldacchini, L. Valdevit, *Opt. Express* **2020**, *28*, 20362.
[38] L. Jiang, W. Xiong, Y. Zhou, Y. Liu, X. Huang, D. Li, T. Baldacchini, L. Jiang, Y. Lu, *Opt. Express* **2016**, *24*, 13687.
[39] J. Rys, S. Steenhusen, C. Schumacher, C. Cronauer, C. Daraio, *Extreme Mech. Lett.* **2019**, *28*, 31.
[40] A. Arslan, W. Steiger, P. Roose, H. Van den Bergen, P. Gruber, E. Zerobin, F. Gantner, O. Guillaume, A. Ovsianikov, S. Van Vlierberghe, P. Dubruel, *Mater. Today* **2021**, *44*, 25.
[41] L. J. Jiang, Y. S. Zhou, W. Xiong, Y. Gao, X. Huang, L. Jiang, T. Baldacchini, J.-F. Silvain, Y. F. Lu, *Opt. Lett.* **2014**, *39*, 3034.
[42] Q. Hu, G. A. Rance, G. F. Trindade, D. Pervan, L. Jiang, A. Foerster, L. Turyanska, C. Tuck, D. J. Irvine, R. Hague, R. D. Wildman, *Addit. Manuf.* **2022**, *51*, 102575.
[43] A. Groetsch, S. Stelzl, Y. Nagel, T. Kochetkova, N. C. Scherrer, A. Ovsianikov, J. Michler, L. Pethö, G. Siqueira, G. Nyström, J. Schwiedrzik, *Small* **2023**, *19*, 2202470.
[44] D. Jang, L. R. Meza, F. Greer, J. R. Greer, *Nat. Mater.* **2013**, *12*, 893.
[45] L. R. Meza, J. R. Greer, *J. Mater. Sci.* **2014**, *49*, 2496.
[46] L. R. Meza, G. P. Phlipot, C. M. Portela, A. Maggi, L. C. Montemayor, A. Comella, D. M. Kochmann, J. R. Greer, *Acta. Mater.* **2017**, *140*, 424.
[47] Z. Vangelatos, G. X. Gu, C. P. Grigoropoulos, *Extreme Mech. Lett.* **2019**, *33*, 100580.
[48] L. R. Meza, A. J. Zelhofer, N. Clarke, A. J. Mateos, D. M. Kochmann, J. R. Greer, *Proc. Natl. Acad. Sci. USA* **2015**, *112*, 11502.
[49] K. Cicha, T. Koch, J. Torgersen, Z. Li, R. Liska, J. Stampfl, *J. Appl. Phys.* **2012**, *112*, 94906.
[50] M. Gernhardt, E. Blasco, M. Hippler, J. Blinco, M. Bastmeyer, M. Wegener, H. Frisch, C. Barner-Kowollik, *Adv. Mater.* **2019**, *31*, 1901269.
[51] L. Chen, Y. Dong, C.-Y. Tang, L. Zhong, W.-C. Law, G. C. P. Tsui, Y. Yang, X. Xie, *ACS Appl. Mater. Interfaces* **2019**, *11*, 19541.
[52] X. Gou, M. Zheng, Y. Zhao, X. Dong, F. Jin, J. Xing, X. Duan, *Appl. Surf. Sci.* **2017**, *416*, 273.
[53] M. Belqat, X. Wu, L. P. C. Gomez, J.-P. Malval, S. Dominici, B. Leuschel, A. Spangenberg, K. Mougin, *Addit. Manuf.* **2021**, *47*, 102232.
[54] M. Dudziak, I. Topolniak, D. Silbernagl, K. Altmann, H. Sturm, R. Garcia, *Nanomaterials* **2021**, *11*, 3285.
[55] M. Lunzer, L. Shi, O. G. Andriotis, P. E. Gruber, A. Markovic, P. J. Thurner, M. Ossipov, R. Liska, A. Ovsianikov, *Angew. Chem., Int. Ed.* **2018**, *57*, 15342.
[56] S. Nakanishi, S. Shoji, S. Kawata, H.-B. Sun, *Appl. Phys. Lett.* **2007**, *91*, 63112.
[57] E. D. Lemma, F. Rizzi, T. Dattoma, B. Spagnolo, L. Sileo, A. Qualtieri, M. De Vittorio, F. Pisanello, *IEEE Trans. Nanotechnol.* **2017**, *16*, 23.
[58] L. Pertoldi, V. Zega, C. Comi, R. Osellame, *J. Appl. Phys.* **2020**, *128*, 175102.
[59] J. Kubacková, C. Slabý, D. Horvath, A. Hovan, G. T. Iványi, G. Vizsnyiczai, L. Kelemen, G. Žoldák, Z. Tomori, G. Bánó, *Nanomaterials* **2021**, *11*, 2961.
[60] Y. Liu, J. H. Campbell, O. Stein, L. Jiang, J. Hund, Y. Lu, *Nanomaterials* **2018**, *8*, 498.
[61] C. M. Portela, B. W. Edwards, D. Veysset, Y. Sun, K. A. Nelson, D. M. Kochmann, J. R. Greer, *Nat. Mater.* **2012**, *20*, 1491.
[62] W. P. Moestopo, S. Shaker, W. Deng, J. R. Greer, *Sci. Adv.* **2023**, *9*, 6725.
[63] Y. Kai, S. Dhulipala, R. Sun, J. Lem, W. DeLima, T. Pezeril, C. M. Portela, *Nature* **2023**, *623*, 514.
[64] H. J. McLennan, A. J. Blanch, S. J. Wallace, L. J. Ritter, S. L. Heinrich, D. K. Gardner, K. R. Dunning, M. J. Gauvin, A. K. Love, J. G. Thompson, *Sci. Rep.* **2023**, *13*, 562.
[65] K. Baglo, M. Sauermoser, M. Lid, T. Paschke, A. B. Afif, M. Lunzer, A. Flaten, M. Steinert, R. Bock, J. Torgersen, *Adv. Mater. Technol.* **2023**, *8*, 2300092.
[66] M. Woletz, F. Chalupa-Gantner, B. Hager, A. Ricke, S. Mohammadi, S. Binder, S. Baudis, A. Ovsianikov, C. Windischberger, Z. Nagy, *Adv. Mater. Technol.* **2024**, *9*, 2300176.
[67] M. Luitz, B. M. Kırpat Konak, A. Sherbaz, R. Prediger, N. Nekoonam, B. Di Ventura, F. Kotz-Helmer, B. E. Rapp, *Adv. Mater. Technol.* **2023**, *8*, 2300667.
[68] S. Zhang, S. Li, X. Wan, J. Ma, N. Li, J. Li, Q. Yin, *Addit. Manuf.* **2021**, *47*, 102358.
[69] C. Cao, J. Liu, X. Xia, X. Shen, Y. Qiu, C. Kuang, X. Liu, *Addit. Manuf.* **2022**, *51*, 102658.
[70] C. Barner-Kowollik, M. Bastmeyer, E. Blasco, G. Delaittre, P. Müller, B. Richter, M. Wegener, *Angew. Chem., Ind. Ed.* **2017**, *56*, 15828.
[71] B. N. L. Costa, R. M. R. Adã, C. Maibohm, A. Accardo, V. F. Cardoso, J. B. Nieder, *ACS Appl. Mater. Interfaces* **2022**, *14*, 13013.
[72] Q. Geng, D. Wang, P. Chen, S.-C. Chen, *Nat. Commun.* **2019**, *10*, 2179.
[73] A. R. Garcia-Taormina, T. Juarez, J. S. Oakdale, J. Biener, A. M. Hodge, *Adv. Eng. Mater.* **2019**, *21*, 1900687.
[74] a) M. P. Jeske, W. Zhang, M. Anthamatten, *Adv. Mater.* **2022**, *7*, 2101725; b) clarified in personal communication with the authors.
[75] ISO 527-2, *Plastics — Determination of Tensile Properties — Part 2: Test Conditions for Moulding and Extrusion Plastics* **2012**, https://www.iso.org/standard/56045.html (accessed: January 2024).
[76] ISO 868, *Plastics and Ebonite — Determination of Indentation Hardness by Means of a Durometer (Shore Hardness)*, **2003**, https://www.iso.org/standard/34804.html (accessed: January 2024).
[77] ISO 2039, *Plastics — Determination of Hardness — Part 1: Ball Indentation Method* **2001**, https://www.iso.org/standard/31264.html (accessed: January 2024).
[78] W. R. Zipfel, R. M. Williams, W. W. Webb, *Nat. Biotechnol.* **2002**, *21*, 1369.
[79] B. Holzer, M. Lunzer, A. Rosspeintner, G. Licari, M. Tromayer, S. Naumov, D. Lumpi, E. Horkel, C. Hametner, A. Ovsianikov, R. Liska, E. Vauthey, J. Fröhlich, *Mol. Syst. Des. Eng.* **2019**, *4*, 437.
[80] D. Helmer, N. Keller, F. Kotz, F. Stolz, C. Greiner, T. M. Nargang, K. Sachsenheimer, B. E. Rapp, *Sci. Rep.* **2017**, *7*, 15078.
[81] J. R. Tumbleston, D. Shirvanyants, N. Ermoshkin, R. Janusziewicz, A. R. Johnson, D. Kelly, K. Chen, R. Pinschmidt, J. P. Rolland, A. Ermoshkin, E. T. Samulski, J. M. DeSimone, *Science* **2015**, *347*, 1349.
[82] S. C. Ligon, R. Liska, J. Stampfl, M. Gurr, R. Mülhaupt, *Chem. Rev.* **2017**, *117*, 10212.
[83] ISO 178, *Plastics—Determination of Flexural Properties* **2019**, https://www.iso.org/standard/70513.html (accessed: January 2024).
[84] P. Gruber, (UpNano GmbH, Vienna), *EP3702132B1*, **2019**.
[85] C. A. Schneider, W. S. Rasband, K. W. Eliceiri, *Nat. Methods* **2012**, *9*, 671.
[86] J. Blaber, B. Adair, A. Antoniou, *Exp. Mech.* **2015**, *55*, 1105.

[87] M. Berardi, K. Gnanachandran, J. Jiang, K. Bielawski, C. W. Visser, M. Lekka, B. I. Akca, *Soft Matter* **2023**, *19*, 615.
[88] S. Bhagwat, A. Goralczyk, M. Luitz, L. Sharieff, S. Kluck, A. Hamza, N. Nekoonam, F. Kotz-Helmer, P. Pezeshkpour, B. E. Rapp, *ACS Appl. Mater. Interfaces* **2023**, *15*, 10109.
[89] Z. Li, N. Pucher, K. Cicha, J. Torgersen, S. C. Ligon, A. Ajami, W. Husinsky, A. Rosspeintner, E. Vauthey, S. Naumov, T. Scherzer, J. Stampfl, R. Liska, *Macromolecules* **2013**, *46*, 352.
[90] R. Whitby, Y. Ben-Tal, R. Macmillan, S. Janssens, S. Raymond, D. Clarke, J. Jin, A. Kay, M. C. Simpson, *RSC Adv.* **2017**, *7*, 13232.
[91] Z. Li, P. Hu, J. Zhu, Y. Gao, X. Xiong, R. Liu, *J. Polym. Sci. A: Polym. Chem.* **2018**, *56*, 2692.
[92] Z. Fang, R. Lu, J. Chen, Q. Zhao, J. Wu, *Add. Manuf.* **2022**, *59*, 103171.
[93] P. Hu, A. Greiner, S. Agarwal, *J. Polym. Sci. A: Polym. Chem.* **2019**, *57*, 752.
[94] M. Idrees, H. Yoon, G. R. Palmese, N. J. Alvarez, *Polymers* **2023**, *15*, 3501.
[95] I. M. Barszczewska-Rybarek, *Materials* **2019**, *12*, 4057.
[96] S. C. Ligon, B. H. Husár, H. Wutzel, R. Holman, R. Liska, *Chem. Rev.* **2014**, *114*, 557.
[97] A. Pikulin, N. Bityurin, V. I. Sokolov, *AIP Adv.* **2015**, *5*, 127215.
[98] T. Baldacchini, C. N. LaFratta, R. A. Farrer, M. C. Teich, B. E. A. Saleh, M. J. Naughton, J. T. Fourkas, *J. Appl. Phys.* **2004**, *95*, 6072.
[99] W. N. Findley, J. S. Lai, K. Onaran, *Creep and Relaxation of Nonlinear Viscoelastic Materials*, North-Holland Publishing, Amsterdam **1976**.
[100] M. Takano, L. E. Nielsen, *J. Appl. Polym. Sci.* **1976**, *20*, 2193.
[101] M. Zamanian, M. Mortezaei, B. Salehnia, J. E. Jam, *Eng. Fract. Mech.* **2013**, *97*, 193.
[102] A. M. Serrano, G. E. Welsch, R. Gibala, *Polym. Eng. Sci.* **1982**, *22*, 946.
[103] D. C. Miller, S. R. Kurtz, *Sol. Energy Mater. Sol. Cells* **2011**, *95*, 2037.
[104] A. Jelinek, S. Zak, M. Alfreider, D. Kiener, *Adv. Eng. Mater.* **2022**, *25*, 2200288.
[105] Y.-S. Lin, C.-J. Yang, *IEEE Access* **2019**, *7*, 71718.
[106] K. Hsiao, B. J. Lee, T. Samuelsen, G. Lipkowitz, J. M. Kronenfeld, D. Ilyn, A. Shih, M. T. Dulay, L. Tate, E. S. G. Shaqfeh, J. M. DeSimone, *Sci. Adv.* **2022**, *8*, eabq2846.
[107] K. Obata, A. El-Tamer, L. Koch, U. Hinze, B. N. Chichkov, *Light: Sci. Appl.* **2013**, *2*, e116.
[108] A. Egner, M. Schrader, S. W. Hell, *Opt. Commun.* **1998**, *153*, 211.
[109] Q. Ge, Z. Li, Z. Wang, K. Kowsari, W. Zhang, X. He, J. Zhou, N. X. Fang, *Int. J. Extreme Manuf.* **2020**, *2*, 022004.
[110] J. T. Toombs, M. Luitz, C. C. Cook, S. Jenne, C. C. Li, B. E. Rapp, F. Kotz-Helmer, H. K. Taylor, *Science* **2022**, *376*, 308.
[111] M. Regehly, Y. Garmshausen, M. Reuter, N. F. König, E. Israel, D. P. Kelly, C.-Y. Chou, K. Koch, B. Asfari, S. Hecht, *Nature* **2020**, *588*, 620.
[112] M. Carlotti, V. Mattoli, *Small* **2019**, *15*, 1902687.